

Unterschrift des Betreuers

DIPLOMARBEIT

Electron Density Perturbations at the Plasma Edge of the ASDEX Upgrade Tokamak

ausgeführt am

Institut für Angewandte Physik
der Technischen Universität Wien

und

Max-Planck-Institut für Plasmaphysik, Garching

unter der Anleitung von

Univ.Prof. Dr. Friedrich Aumayr

Univ.Do. Dr. Elisabeth Wolfrum

durch

Florian Martin Laggner, BSc

Sittich 8a
9560 Feldkirchen

Wien, 2013

Unterschrift

Abstract

In future fusion devices, the particle transport towards the plasma facing components (PFCs) is crucial. Large particle flows lead to faster degradation of the materials, resulting in large maintenance expense and therefore, uneconomical power plants. So-called blob-filaments, which are intermittently released density perturbations at the plasma edge, transport plasma particles through the scrape off layer (SOL) towards the wall. A deeper understanding of the generation and propagation of these blob-filaments is required to ensure low particle fluxes on the PFCs.

At the axial symmetric divertor experiment upgrade (ASDEX Upgrade) tokamak, the plasma edge electron density (n_e) is well probed by a lithium beam (LB) diagnostic. The diagnostic is based on the interaction of a neutral LB and the plasma particles. The emitted Li I (2p \rightarrow 2s) line radiation is depending on n_e . In the frame of this thesis, the sensitivity of the LB diagnostic is investigated by numerical simulation of artificial n_e perturbations on background n_e profiles. The corresponding line radiation profiles are calculated and analysed. The essential result is that in the SOL the perturbations are well resolvable in amplitude and size, giving the LB diagnostic the ability to measure velocities and sizes of blob-filaments. Furthermore, the relation between the n_e perturbation amplitude (or size) and the line radiation perturbation amplitude (or size) is almost linear.

Statistical data analysis methods as conditional averaging and cross correlation analysis are applied to the artificial and measured line radiation profiles to determine blob-filament sizes. Owing to the lifetime of the Li(2p)state, the line radiation profiles are smeared. Using a Richardson-Lucy algorithm, this smearing can be deconvolved, enabling the direct determination of radial positions and sizes of blob-filaments from conditionally averaged line radiation profiles.

A series of plasma discharges, varying the magnetic field B , is performed to investigate the relation between the most stable blob-filament size (δ_*) and B . Surprisingly, the blob-filament sizes, which are determined by cross correlation analysis, are about a factor of three larger, than the sizes δ_* predicted from theory. The $B^{-4/5}$ dependence of δ_* from the theoretical blob model is not reproduced by the measurements.

Kurzfassung

In zukünftigen Fusionsanlagen ist der Teilchentransport auf Plasma-belastete Komponenten (Wandmaterialien) entscheidend. Große Teilchenströme führen zu schnellerer Degradierung der Wandmaterialien, die einen größeren Wartungsaufwand bedingen, was wiederum zu unwirtschaftlichen Fusionskraftwerken führt. Sogenannte Blob-Filamente sind stoßweise auftretende Dichteschwankungen am Plasmarand, die Plasma-Teilchen durch die Abschältschicht auf die Wand transportieren. Ein genaueres Verständnis über die Entstehung und Bewegung der Blob-Filamente ist erforderlich um niedrige Teilchenströme auf die Wandmaterialien zu garantieren.

Am axialsymmetrischen Divertor Experiment Upgrade (ASDEX Upgrade) Tokamak ist die Elektronendichte am Plasmarand mittels einer Lithiumstrahl-Diagnostik gut messbar. Diese Diagnostik basiert auf der Wechselwirkung zwischen einem Strahl von elektrisch neutralen Lithium Atomen und den Teilchen des Plasmas. Die dabei emittierte Li I ($2p \rightarrow 2s$) Linienstrahlung ist abhängig von der Elektronendichte des Plasmas. Im Rahmen dieser Arbeit wird die Empfindlichkeit der Lithiumstrahl-Diagnostik durch numerische Simulation von generierten Elektronendichteschwankungen auf Hintergrunddichteprofilen untersucht. Die zugehörigen Linienstrahlungsprofile werden berechnet und analysiert. Das wesentliche Ergebnis ist, dass Elektronendichteschwankungen, die in der Abschältschicht auftreten, mit guter Auflösung von Amplitude und Breite beobachtet werden können. Das gibt der Lithiumstrahl-Diagnostik die Fähigkeit, Geschwindigkeiten und Größen von Blob-Filamenten zu messen. Darüber hinaus ergibt sich eine beinahe lineare Relation zwischen Elektronendichteschwankungsamplitude (oder -größe) und Amplitude (oder Größe) der Schwankung im Linienstrahlungsprofil.

Statistische Methoden zur Datenanalyse, wie das konditionierte Mitteln und Kreuzkorrelationsanalysen, werden auf generierte und gemessene Linienstrahlungsprofile angewendet, um die Größen von Blob-Filamenten zu bestimmen. Durch die Lebensdauer des Li($2p$)-Zustandes werden die Linienstrahlungsprofile verschmiert. Mittels eines Richardson-Lucy Algorithmus kann diese Verschmierung entfaltet werden, was die direkte Bestimmung der radialen Position von Blob-Filamenten und deren Größe von konditionell gemittelten Linienstrahlungsprofilen ermöglicht.

Eine Serie von Plasmaentladungen mit variiertem Magnetfeld B wurde durchgeführt um den Zusammenhang zwischen der stabilsten Größe von Blob-Filamenten (δ_*) und B zu untersuchen. Erstaunlicherweise sind die durch Kreuzkorrelationsanalyse ermittelten Blob-Filament-Größen um einen Faktor drei größer als die theoretisch vorhergesagten Größen δ_* . Die $B^{-4/5}$ Abhängigkeit von δ_* des theoretischen Blob-Modells wird von den Messungen nicht reproduziert.

List of publications

Parts of this thesis have already been published or are accepted for publication.

Publications in Scientific Journals

- M. Willensdorfer, G. Birkenmeier, R. Fischer, F. M. Laggner, E. Wolfrum, G. Veres, F. Aumayr, D. Carralero, T. Kobayashi and the ASDEX Upgrade Team
"Characterization of the lithium beam emission spectroscopy at ASDEX Upgrade"; accepted in *Plasma Phys. Control. Fusion* (2013)
- G. Birkenmeier, F. M. Laggner, M. Willensdorfer, T. Kobayashi, P. Manz, E. Wolfrum, D. Carralero, R. Fischer, B. Sieglin, G. Fuchert, U. Stroth and the ASDEX Upgrade Team
"Magnetic field dependence of the blob dynamics in the edge of ASDEX Upgrade L-mode plasmas"; in preparation (2013)

Conference contributions

- F. M. Laggner, E. Wolfrum, M. Willensdorfer, G. Birkenmeier, T. Kobayashi, F. Aumayr and the ASDEX Upgrade Team
Poster: "Reconstruction of electron density perturbations using lithium beam emission spectroscopy"; DPG Frühjahrstagung, Jena, Germany, P10.5 (2013)
- G. Birkenmeier, T. Kobayashi, F. M. Laggner, M. Willensdorfer, E. Wolfrum, D. Carralero, P. Manz, H. W. Müller, R. Fischer, U. Stroth and the ASDEX Upgrade Team
Poster: "Investigations of the magnetic field dependence of blob velocity and size with Li-BES at ASDEX Upgrade"; 39th EPS Conference on Plasma Physics, Espoo, Finland; Proceedings: Europhys. Conf. Abstracts, **37D**, 5.105 (2013)

Contents

1	Introduction	1
1.1	Nuclear fusion	1
1.2	Magnetic confinement fusion	3
1.2.1	Tokamak Concept	3
1.2.2	ASDEX Upgrade	4
1.3	Objectives of this thesis	5
2	Blob-Filaments	7
2.1	Theoretical blob model	7
2.1.1	Blob formation and propagation	8
2.1.2	Scaling of fluctuation level and blob size	9
2.1.3	Difference between blobs and ELMs	10
2.2	Diagnostic methods for blob observation	10
2.3	Statistical tools for blob observation	11
2.3.1	Correlation Function	11
2.3.2	Conditional Average	13
3	Lithium beam diagnostics	15
3.1	Experimental setup of the lithium beam (LB) diagnostic	15
3.1.1	LB diagnostic upgrade	16
3.2	Lithium beam impact excitation spectroscopy	18
4	Sensitivity Study	20
4.1	Method	20
4.1.1	Generation of artificial electron density profiles	21
4.1.2	Shaping of electron density perturbations	21
4.2	Effects of electron density perturbations on emission profiles	22
4.3	Emission response on perturbation amplitude	26
4.4	Emission response on perturbation width	27

5	Richardson-Lucy Deconvolution	31
5.1	Li(2p) lifetime induced smearing	31
5.2	Richardson-Lucy algorithm	32
5.2.1	Adaptation and numerical implementation of the algorithm . . .	34
5.2.2	Application on artificial emission profiles	35
5.3	Implementation of LOS positions	36
5.3.1	Deconvolution of sampled profiles	37
6	Blob Size Measurement	40
6.1	Flux Coordinates	40
6.2	Perturbation reconstruction using conditional averaging	41
6.3	Correlation analysis of evaluated electron density profiles	44
6.4	Blob size determination by correlation analysis	48
6.4.1	Discharge layout	48
6.4.2	Spatio-temporal resolution of blob-filaments	51
6.4.3	Simulation of density perturbations on a mean evaluated density profile	53
6.4.4	Comparison with measured data	55
6.4.5	Relation between width of the emission profile perturbation and the blob size	57
6.4.6	Magnetic field dependence of the blob-filament size	58
7	Summary	61
7.1	Main results	61
7.1.1	Capabilities of the LB diagnostic	61
7.1.2	Blob size analysis	62
7.2	Future perspectives	62
	Acronyms	64
	Acknowledgement	66
	Bibliography	68

Chapter 1

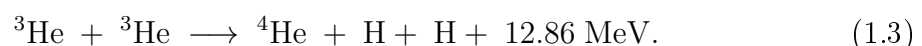
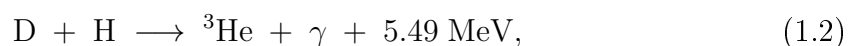
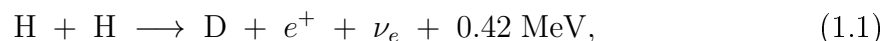
Introduction

Energy, indispensable for economy, is an important basis for human wealth. Owing to the fast growing economies in populous countries e.g. China or India, the global energy demand will continuously increase in the future. In contrast, fossil fuels, which are commonly used for energy production, will become less accessible or even will be depleted within the next decades. Furthermore, the burning of fossil fuels produces huge amounts of carbon dioxide, a green house gas, which is proven to have negative influences on the world's climate [1].

These problems have to be solved to maintain the high standard of living in the Western countries and moreover, improve the standard of living for all humankind. Therefore, the development of alternatives for energy production is an important challenge in this century. Nuclear fusion, a reaction releasing high amounts of energy, could contribute to the world's future power supply.

1.1 Nuclear fusion

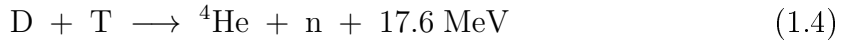
In a fusion process, light atomic nuclei are combined to heavier ones. The mass difference between the sum of the masses from the light nuclei and the masses of the fusion products is transformed to energy, corresponding to the Einstein's equivalence of energy and mass: $E = mc^2$. These processes have been the energy source of the sun for several billions of years. The main fusion reactions in the sun's core are:



Two protons (equivalent to hydrogen (H) nuclei) combine and form a deuterium (D) nucleus (equation 1.1). In the following the D nucleus fuses with another proton to

helium-3 (^3He) (equation 1.2). Finally, two ^3He nuclei fuse, generating a helium (^4He) nucleus (equivalent to an alpha particle) and two H nuclei (equation 1.3). Each reaction releases energy in the range of MeVs, making nuclear fusion to one of the most powerful energy sources.

For the last decades the aim of fusion research has been to access this energy source for electric power production. Conditions as in the core of the sun, especially the high densities, can not be realized at large time scales on earth. Therefore, a more efficient fusion reaction will be used for this purpose:



In the so-called D-T reaction a deuterium (D) and a tritium (T) nucleus are fusing to helium (^4He) with the release of a neutron (n), delivering in total 17.6 MeV of kinetic energy on the two fusion products. Due to kinematics the kinetic energy is apportioned to 3.5 MeV on the ^4He nucleus and 14.1 MeV on the neutron. The reason to use this fusion reaction is that it has a significantly higher cross section at (for fusion) relatively low energies. Figure 1.1 shows the temperature¹ dependence of the cross section from three fusion reactions. It is clearly demonstrated that the cross section of the D-T reaction (red curve) is about two orders of magnitude higher in the temperature range 10-100 keV than the cross section of the D-D or D- ^3He reaction. In terms of temperature these energies still correspond to millions of Kelvin. At such temperatures atoms are in the state of plasma, which means that they are fully ionized.

To achieve high fusion reaction rates, the particles have to collide many times, because the cross section for Coulomb repulsion is higher than the cross section for fusion. The average nucleus has to collide about 50 times till it fuses. Therefore, the confinement of the plasma particles in the reaction volume has to be sufficiently good. The Lawson criterion gives a threshold for a self-sustaining fusion reaction [4]. For the D-T fusion reaction, the product of plasma density, energy confinement time and temperature has to be higher than $5 \cdot 10^{21} \text{ keV} \cdot \text{s} / \text{m}^3$.

There are two main approaches to achieve the criterion: One is to increase the density to very large values which automatically reduces the energy confinement time, owing to the Coulomb repulsion of the particles. This concept is used in inertial confinement fusion [5], where frozen gas pellets are compressed with laser or ion beams. The other possibility is to enlarge the energy confinement time by means of electromagnetic fields, operating at lower plasma densities. This approach is utilized in magnetic confinement fusion.

¹The temperature equivalent of 1 keV is 11 605 000 K.

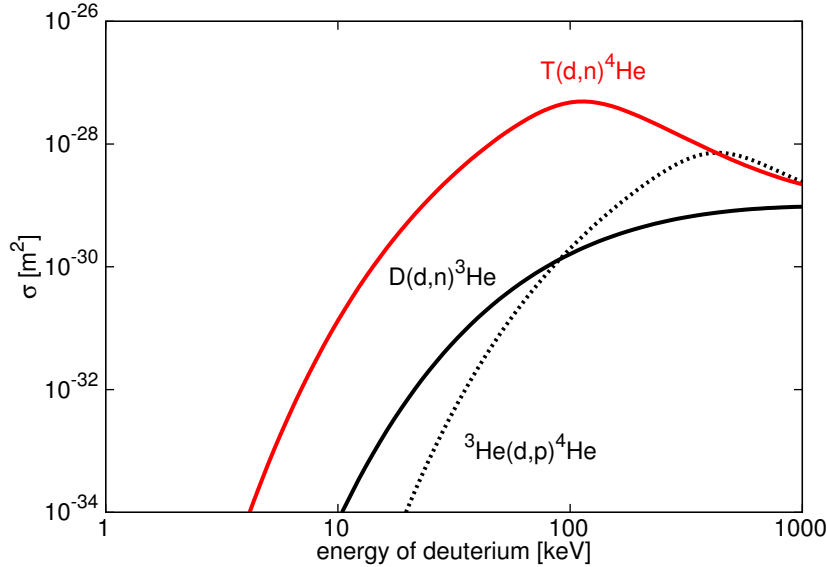


Figure 1.1: Cross sections for several fusion reactions; The D-T fusion reaction ($T(d,n)^4\text{He}$) has a significantly higher cross section at low energies than the D-D ($D(d,n)^3\text{He}$) or D- ^3He ($^3\text{He}(d,n)^4\text{He}$) reaction. Curves taken from [2, 3].

1.2 Magnetic confinement fusion

Owing to full ionisation in a fusion plasma, all plasma particles are charged and therefore, they are sensitive to magnetic fields. Several approaches to confine fusion plasmas with magnetic fields have been developed since the 1950s. A promising and mature concept for magnetic confinement fusion is the tokamak.

1.2.1 Tokamak Concept

The word tokamak is a Russian abbreviation and means toroidal chamber with magnetic coils. Figure 1.2a shows a schematic drawing of a tokamak. It consists of toroidally assembled magnetic field coils (blue coils, figure 1.2a) creating a toroidal magnetic field. This field alone and the resulting drifts in the plasma would result in an unstable plasma configuration, leading to no confinement. To reach a stable plasma configuration the magnetic field lines have to be twisted around the torus. Therefore, a poloidal magnetic field (green arrows, figure 1.2a) is applied. The poloidal field is created via induction of a current in the plasma with the inner poloidal field coils (green coils, figure 1.2a). This coil represents the primary circuit of a transformer, whereas the secondary circuit is the plasma itself. The combination of the toroidal and the poloidal magnetic field leads to field lines which run helically around the torus (dark blue arrow, figure 1.2a). The necessity of the induced plasma current limits the

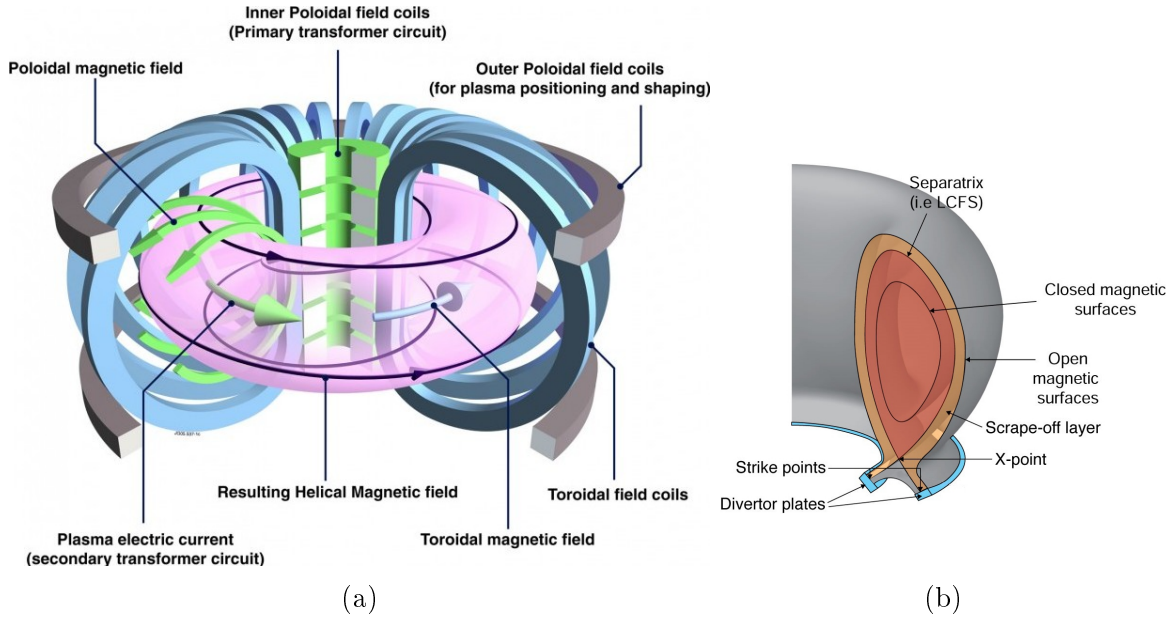


Figure 1.2: (a) Magnetic coils and fields in a tokamak; Figure taken from [6].
 (b) Poloidal cross section of a tokamak divertor plasma; Figure adapted from [7]

discharge duration of a tokamak. Accordingly, tokamaks typically only operate in pulsed mode and not in steady state operation.

ITER (the Latin word for "the way"), a fusion experiment at large scale, is currently constructed in southern France. Its aim is to demonstrate the possibility to build and operate a fusion experiment, which produces ten times more energy than required for the plasma heating. Since the tokamak concept is the most investigated and most developed magnetic fusion configuration, ITER will be a tokamak.

1.2.2 ASDEX Upgrade

The axial symmetric divertor experiment upgrade (ASDEX Upgrade) is a medium sized tokamak experiment. It is operated by the Max Planck Institute for Plasma Physics (IPP), located in Garching near Munich, Germany. Table 1.1 gives an overview of the design parameters. The divertor (figure 1.2b) of ASDEX Upgrade enables a specific power dissipation and helps to remove plasma impurities from the core plasma. This feature allows an easier access to the high confinement mode (H-mode), which is the intended operation mode for ITER. The H-mode was discovered in the ASDEX tokamak [9], the parent experiment of ASDEX Upgrade and is characterized by steep gradients in the plasma edge density and temperature profiles, which are caused by an edge transport barrier (ETB) [10]. These increased gradients at the plasma edge are called pedestal. At ASDEX Upgrade the pedestal width is about

technical data	
maximum toroidal magnetic field (\mathbf{B}_t)	3.2 T
plasma current I_p	0.4 MA - 1.6 MA
plasma heating power (P_{heat})	up to 27 MW
plasma parameters	
major plasma radius R_0	1.65 m
minor plasma radius a	0.5 m
plasma volume	14 m ³
plasma mass	3 mg

Table 1.1: Design parameters of ASDEX Upgrade [8]

1.5 cm [11], which is only 3% of the minor plasma radius. In this region the plasma density and temperature change by one order of magnitude and the main physical processes for the transition to the H-mode are believed to be located there. To investigate the pedestal, accurate plasma edge diagnostics are required. At ASDEX Upgrade this region is well probed, using several diagnostic methods e.g. Thomson scattering (TS) or lithium beam emission spectroscopy (Li-BES).

1.3 Objectives of this thesis

The lithium beam (LB) diagnostic (see chapter 3) at ASDEX Upgrade is routinely used to measure electron density (n_e) profiles at the plasma edge. A recently installed diagnostics upgrade [12, 13] increases the temporal resolution and the photon yield, enabling n_e fluctuation measurements. Density fluctuations are caused by plasma turbulence, which is the dominating transport phenomenon in the plasma core as well as in the scrape off layer (SOL). In contrast to the core (confined plasma region), where the magnetic field lines are closed, the SOL is the region, where the magnetic field lines are open, ending at plasma facing components (PFCs) (c.f. figure 1.2b). In the SOL large, magnetic field aligned n_e fluctuations occur, so-called blob-filaments [14]. Blob-filaments (see chapter 2) are strongly localized perpendicular to the magnetic field and denser than the background plasma. Owing to external forces, blobs become charge polarized and the resulting $\mathbf{E} \times \mathbf{B}$ drift moves them radially outward. Hence, blobs contribute to the radial convective transport. Radially transported plasma can degrade the first wall and therefore, an understanding of the generation and propagation of blobs is relevant for ITER and future fusion power plants.

The main aims of this thesis are to quantify the capabilities of the LB diagnostic (see chapter 3) at ASDEX Upgrade for n_e fluctuation measurements and to perform first tests of turbulence analysis on experimental data:

- A sensitivity study on the resolvability of n_e perturbations is performed. The effects of artificial n_e perturbations on the Li I (2p \rightarrow 2s) line radiation profiles are investigated via forward modelling, varying the perturbation amplitude, spatial size and position. (see chapter 4).
- The smearing of the line radiation profiles, which is caused by the lifetime of the excited Li(2p) state, is studied. To achieve a higher radial accuracy for localizing the perturbation position from the line radiation profile, a Richardson-Lucy algorithm is applied to the artificial Li I (2p \rightarrow 2s) line radiation profiles (see chapter 5).
- Large n_e perturbations in the SOL (blob-filaments) are experimentally investigated, using conditionally averaged line radiation profiles (see chapter 6.2).
- Blob-filament sizes are determined from Li I (2p \rightarrow 2s) line radiation profiles, using the cross correlation function. The dependency of their size on the magnetic field (B) is studied and compared with theoretical predictions (see chapter 6.4).

Chapter 2

Blob-Filaments

A typical plasma density profile (chapter 4.1.1, c.f. figure 4.1) is rather flat in the core. Towards the separatrix, it slowly decreases. At the plasma edge it has a stronger gradient and in the SOL it is flat again. A mathematical function, which is often used to describe the profile shape is the hyperbolic tangent (\tanh) [15]. In low confinement mode (L-mode), the occurring density profile gradients can only be explained by turbulent transport [16, 17]. The H-mode is characterized by steep gradients at the plasma edge (the so-called pedestal). It is formed by an ETB, which suppresses the turbulence. In L-mode and in H-mode (in between edge localized modes (ELMs)), intermittent plasma transport is observed. These plasma filaments (or blob-filaments) are easily accessible for measurements, because of their size (in the range of a few centimetres).

This chapter will give a brief introduction to blob-filaments or short blobs. Hereafter, these two terms will be used interchangeably. In the first section 2.1 theoretical blob models are described, later, the statistical data analysis methods to detect blob-filaments are discussed (sections 2.2, 2.3).

2.1 Theoretical blob model

Three necessary criteria have to be satisfied to fulfil the basic definition of a blob-filament [14]. These criteria are derived from a theoretical base model which is described in section 2.1.1:

1. A blob is considerably denser, usually two to three times at the peak value, than the surrounding background density. Furthermore, its density distribution has a single peak.
2. It is aligned parallel to magnetic field \mathbf{B} and its density variation parallel to \mathbf{B} is orders of magnitude less than its change perpendicular to \mathbf{B} .
3. Its propagation is dominated by the $\mathbf{E} \times \mathbf{B}$ velocity in the direction of a charge polarizing force (discussed in section 2.1.1).

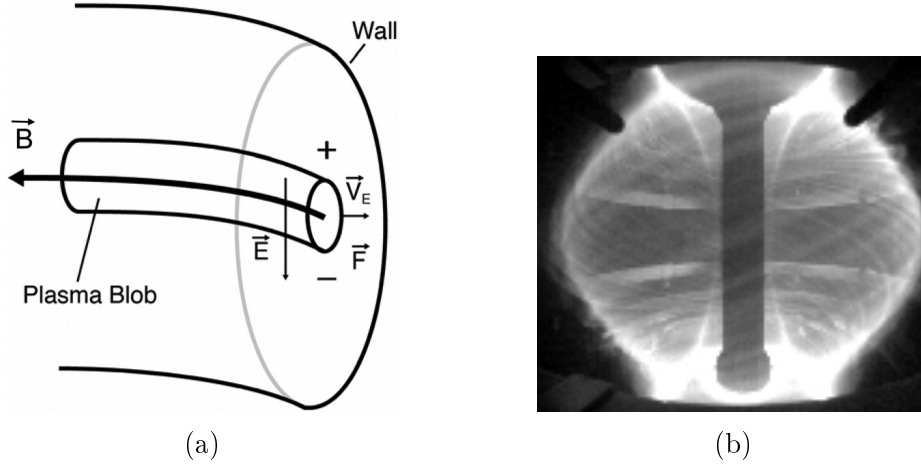


Figure 2.1: (a) Sketch of a blob-filament showing the forces leading to radial transport; Figure taken from [14]. (b) Fast camera image from L-mode filaments in MAST; Image taken from [18]

A sketch of a plasma blob is shown in figure 2.1a. Blob-filaments have been observed in several magnetic configurations as in linear plasma devices, tokamaks or stellarators. A table of references is given in reference [14]. These observations suggest that the generation of blob-filaments is almost independent of the magnetic field geometry. To explain the formation and propagation of blob-filaments, a general model can be applied.

2.1.1 Blob formation and propagation

The basic blob model [19–21] assumes a magnetic field aligned density perturbation in the plane perpendicular to \mathbf{B} (c.f. figure 2.1a). A species summed force \mathbf{F} acts on the density perturbation. It contains forces, which occur in linear or in toroidal magnetic field configurations, e.g. for linear plasmas the neutral friction force or centrifugal force for rotating linear plasmas. In tokamak plasmas, the dominating terms in the species summed force \mathbf{F} are the curvature and the ∇B force ($B = |\mathbf{B}|$). The outward directed $-\nabla B$ leads to the drift velocity:

$$\mathbf{v}_{\nabla B} = -\frac{W_{\perp}}{q} \frac{\nabla_{\perp} B \times \mathbf{B}}{B^3}. \quad (2.1)$$

W_{\perp} denotes the energy for the motion perpendicular to \mathbf{B} . ∇_{\perp} is the gradient component, which is perpendicular to the field line, and q is the charge of the plasma particle. The direction of $v_{\nabla B}$ is dependent on the sign of q . Therefore, the negatively charged particles (electrons) move downwards and the positively charged particles (nuclei) move upwards, leading to a charge separation of the density perturbation. The separated charges create a vertical electric field \mathbf{E} . This field creates, in combination with

\mathbf{B} , an $\mathbf{E} \times \mathbf{B}$ drift with the velocity

$$\mathbf{v}_{\mathbf{E}} = \frac{\mathbf{E} \times \mathbf{B}}{B^2}. \quad (2.2)$$

The drift velocity $\mathbf{v}_{\mathbf{E}}$ is independent of the particle charge, which leads to a movement of the complete density perturbation in the direction of \mathbf{F} . In the discussed case of the ∇B force, the direction is $-\nabla B$, which corresponds to an outward propagation of the density perturbation.

2.1.2 Scaling of fluctuation level and blob size

To validate and estimate turbulent transport properties in plasmas, scaling laws are derived. E.g. several measurements show a dependency of the fluctuation level $\delta n/n$ on the magnetic field \mathbf{B}

$$\delta n/n \propto \mathbf{B}^{-\alpha}, \quad (2.3)$$

where α is in the range from 0.5 – 1.0 [22] or 0.5 – 0.9 [23] for SOL turbulence in toroidal plasmas.

Sheath-limited blob models propose, that the stability of the blob is dependent on the blob size δ_b [14, 24], assuming a Gaussian shaped density distribution

$$n_b(x) \propto e^{-\left(\frac{x}{\delta_*}\right)^2} \quad (2.4)$$

Small blobs are transformed into mushroom-like structures, owing to the Kelvin-Helmholtz instability. Large blobs form fingers, which are caused by the interchange instability. Only for blob sizes $\delta_b \sim \delta_*$, stable blobs are formed, which can travel distances of several centimetres. At this blob size, the terms of the underlying differential equations are balanced. Detailed information on the derivation of the most stable blob size δ_* can be found in reference [24]. It is given by

$$\delta_* = \rho_s^{4/5} L_{\parallel}^{2/5} / R^{1/5}. \quad (2.5)$$

δ_* is dependent on the parallel connection length L_{\parallel} , the major radius R and the sound Larmor radius

$$\rho_s = \frac{\sqrt{m_i T_e}}{eB}, \quad (2.6)$$

with the ion mass m_i , the electron temperature T_e , the unit electric charge e and the absolute value of the magnetic field B . Therefore, δ_* is proportional to the magnetic field:

$$\delta_* \propto B^{-4/5}. \quad (2.7)$$

This dependency is also used in reference [25], where numerical propagation analyses of blobs are done. Within this thesis the dependency of the spatial blob size on the magnetic field is investigated (c.f. chapter 6.4.6).

2.1.3 Difference between blobs and ELMs

Theory and simulations predict that blob-filaments and ELMs [26] originate from non-linear saturation processes of edge turbulence or coherent magnetohydrodynamic (MHD) instabilities. Although, the physics behind the generation of them is most likely not the same [14, 18], it is proven that ELMs produce filaments that propagate through the far SOL, in a similar way to blobs.

In comparison to a blob, ELM filaments are larger in their cross-section perpendicular to \mathbf{B} . The plasma of an ELM is denser and hotter owing to its birth region at the pedestal top, where the temperature and density are larger than in the separatrix region. Furthermore, ELMs carry significant parallel current [27], detectable easily by magnetic pick up coils, which is at the moment not possible for blobs. There is experimental evidence that ELM footprints can remain connected to the hot dense plasma as the filament begins moving through the SOL.

2.2 Diagnostic methods for blob observation

Intermittent structures at the plasma edge have been observed by probe and optical diagnostics in several tokamak and other devices [14, 28], e.g. figure 2.1b shows a fast camera image from L-mode filaments in MAST.

One way to resolve intermittent plasma structures are Langmuir probes, which measure e.g. the ion saturation current. Statistical analyses of ion saturation currents show their non-Gaussian and intermittent character. A detailed description on statistical methods for blob analysis is given in section 2.3. Probe arrays can be used to determine blob sizes, propagation directions and velocities. Two main diagnostic issues with Langmuir probe data have to be considered; the theory for Langmuir probes in magnetic fields is still incomplete and therefore, a quantitative interpretation is difficult. Furthermore, the influence of the probe on the plasma, e.g. through perturbing effects, is unclear [29].

Another possibility to observe filament structures is visible light emission from background neutrals due to electron excitation. The method was used in reference [18] to obtain the image in figure 2.1b. Active optical diagnostics are either using beam emission spectroscopy (BES), e.g. at DIII-D [30] and at the tokamak experiment for technology oriented research (TEXTOR) [31], or gas puff imaging (GPI), e.g. at Alcator C-Mod [32] and at the national spherical torus experiment (NSTX) [33].

Both methods use neutral atoms, BES a neutralized atomic beam, GPI a neutral gas puff, to generate line radiation and detect it with optical systems. These methods allow 2D-images of the turbulent structures.

2.3 Statistical tools for blob observation

To investigate turbulent structures in the plasma, high spatial and temporal resolution is necessary. The LB diagnostic at ASDEX Upgrade fulfils these requirements. A detailed description of its setup is given in chapter 3.

In order to determine size, velocity and lifetime of blob-filaments, several statistical methods, applied to fluctuation data, are required. These are introduced in the following.

2.3.1 Correlation Function

To resolve characteristic spatial scales in turbulence data, cross correlation analysis can be utilized. The cross correlation function CC_{xy} of two time traces $x(t)$ and $y(t)$ with zero arithmetic mean is calculated by

$$CC_{xy}(\Delta t) = \frac{CV_{xy}(\Delta t)}{\sigma_x \sigma_y}, \quad (2.8)$$

using the time lag Δt (c.f. figure 2.2a), the standard deviations σ_x , σ_y (of $x(t)$ and $y(t)$) and the covariance

$$CV_{xy}(\Delta t) = \langle x(t)y(t + \Delta t) \rangle. \quad (2.9)$$

The expectation value is denoted with $\langle \cdot \rangle$. Owing to the assumption of ergodicity, the expectation value can be calculated as the time average [34, 35]. The maximum of the cross correlation function $CC_{xy}(\Delta t)$ is 1, if the information of signal $x(t)$ occurs identically at signal $y(t)$ at a later point in time $t + \Delta t$. So-called ‘anti-correlation’ is observed for $CC_{xy}(\Delta t) = -1$, i.e. $x(t) \propto -y(t + \Delta t)$. Differences in the information content of $x(t)$ and $y(t)$, and signal noise, which is intrinsic in measurements, lead to a decorrelation of $x(t)$ and $y(t)$, resulting in maximum values of $|CC_{xy}| < 1$.

For locally separated time traces $x_i(t)$ (at different positions i) the cross correlation transforms to spatial cross correlation function

$$CC_{ij}(\Delta t) = \frac{\langle x_j(t)x_i(t + \Delta t) \rangle}{\sigma_j \sigma_i} \quad (2.10)$$

using a chosen reference signal $x_j(t)$ at position j . It can be plotted two-dimensionally in space i and time Δt , to determine spatio-temporal patterns of quasi-coherent structures of the fluctuating signals. This method is used in reference [36] for Langmuir probe data. In chapter 6.4, correlation analysis is utilized in an extended form to determine radial blob sizes.

Owing to a higher noise level from BES data in comparison to Langmuir probe data,

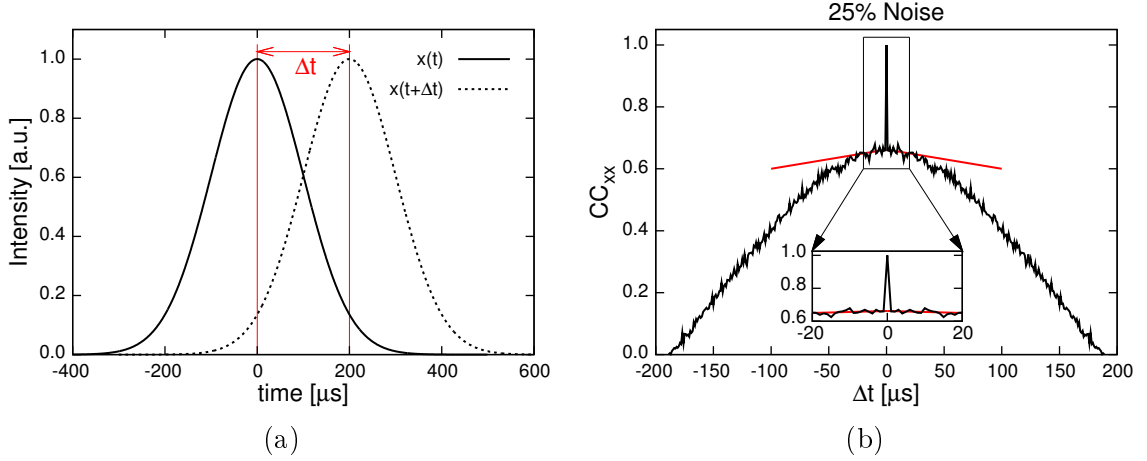


Figure 2.2: (a) Gaussian-shaped signal ($x(t)$) which is shifted by a time lag of Δt . (b) Autocorrelation function of the signal from (a) which was distorted by 25% random Gaussian-distributed noise. At $\Delta t = 0$ the ‘noise peak’ is observed. To remove it, seven adjacent values (for both signs of Δt) are linearly interpolated (red lines; extended to larger Δt for visibility).

it is necessary to separate the desired signal from the intrinsic photon noise. The cross correlation function CC_{xy} becomes the autocorrelation function CC_{xx} , if $x(t) = y(t) \forall t$ (c.f. figure 2.2a). The autocorrelation function is usable to determine the noise level of a signal $x(t)$ and to remove the ‘noise peak’ [37], which is formed due to the incoherent structure of noise. This is reflected by a significantly smaller correlation time of the noise than the correlation time of the desired (noise-free) signal. Figure 2.2b explains this point in detail. If $\Delta t = 0$, the noise fully contributes to the autocorrelation function. For values of $\Delta t \neq 0$, this contribution is strongly reduced owing to the incoherent nature of noise and the residual part in the autocorrelation function is from the desired signal, which shows correlation at larger timescales. Therefore, a peak in the autocorrelation function is formed at $\Delta t = 0$, which is called ‘noise peak’.

This peak and moreover, the noise contribution can be removed from the autocorrelation function. A method, which can be applied for this purpose, is suggested in reference [37]. Via linear interpolation of adjacent values, the magnitude of the autocorrelation function at zero time lag without noise contribution is estimated. In figure 2.2b seven adjacent values of the autocorrelation function from positive time lags and seven from negative time lags are interpolated. The interpolation lines are plotted in red (for visibility they are extended to larger values of Δt). A zoom-in shows the autocorrelation function close to the ‘noise-peak’ in detail.

The autocorrelation function CC_{xx} is by definition the autocovariance CV_{xx} normalized to the standard deviation (see equation 2.8) and for this reason always 1 at $\Delta t = 0$. To determine the actual standard deviation of the noise-free signal, the autocovariance CV_{xx} has to be utilized instead of the autocorrelation CC_{xx} . The

‘noise-peak’ removed CV_{xx} at $\Delta t = 0$ is the variance of the noisefree signal and therefore, the standard deviation of the noisefree signal can be determined by the square root of the ‘noise-peak’ removed $CV_{xx}(0)$.

To analyse spatial correlation lengths either the spatial cross correlation CC_{ij} or the spatial cross covariance CV_{ij} can be used as long as the subtraction of the ‘noise peak’ (from the autocorrelation/covariance function) is done precisely, making a criterion like the full width at half maximum (FWHM) applicable. If different and large noise levels occur at the channels x_i and x_j , the spatial cross covariance CV_{ij} is the better choice, because it is not normalized to the standard deviation of the signals. At large noise levels, the signal’s standard deviation is dominated by the noise amplitude. Therefore, the normalization of the CC_{ij} is more or less to the standard deviation of the noise and not to the standard deviation of the noisefree signals.

2.3.2 Conditional Average

Cross correlation determines the correlation between two signals $x(t)$ and $y(t)$, although it gives no information about signal amplitudes and their signs. To analyse these quantities and to reduce noise, the conditional average is an appropriate method [38]. A reference signal $x(t)$ is chosen and a condition is defined, e.g. a deviation of the signal amplitude from the mean, which is higher than several times the standard deviation σ_x . If this condition is fulfilled at a certain time τ_1 , the signal $x(t)$ is stored for a small time interval

$$X_1 = \{x(t) | t \in [\tau_1 - \Delta t, \tau_1 + \Delta t]\}. \quad (2.11)$$

At the same time point (τ_1) and interval length ($2\Delta t$) the second signal $y(t)$ is also stored

$$Y_1 = \{y(t) | t \in [\tau_1 - \Delta t, \tau_1 + \Delta t]\}. \quad (2.12)$$

This routine is applied to all points in time τ_i ($i \in [2, M]$), where the condition is fulfilled, leading to M sub-intervals X_i from $x(t)$ and M sub-intervals Y_i of $y(t)$. In the following, the average of these time traces is composed

$$\bar{X}(t) = \frac{1}{M} \sum_{i=1}^M X_i, t \in [-\Delta t, \Delta t]. \quad (2.13)$$

$$\bar{Y}(t) = \frac{1}{M} \sum_{i=1}^M Y_i, t \in [-\Delta t, \Delta t]. \quad (2.14)$$

Because of the condition, which generates the sub-intervals, it is called the conditional average. Is there a characteristic structure in $y(t)$ at time points τ_i , which is higher than the noise, it might also appear in the averaged value $\bar{Y}(t)$. Contributions from noise are removed by the average. If this structure synchronously appears in $x(t)$ at

the same time τ_i , it can also be observed in $\overline{X}(t)$.

The conditional average method is applied in chapter 6.2 to reconstruct mean n_e perturbations directly from line radiation profiles. Furthermore, the conditionally averaged line radiation profiles are used to demonstrate the abilities of the Richardson-Lucy algorithm to remove the Li(2p) lifetime induced smearing (see chapter 5).

Chapter 3

Lithium beam diagnostics

The LB diagnostic is based on the interaction between plasma particles and a neutral beam of lithium (Li) atoms [39–48]. Thereby, the Li atoms get either ionized, excited or de-excited by collisions with the plasma particles. Excited atomic states de-excite after a certain lifetime, emitting characteristic line radiation.

The Li(2p) state gets most populated due to the interactions between plasma particles and Li atoms. It de-excites after ~ 27 ns to the Li(2s) state, emitting Li I (2p \rightarrow 2s) line radiation at a characteristic wavelength of 670.8 nm. The intensity of the line radiation is detected with an optical observation system along the beam. From the line radiation profile, the electron density profile can be calculated. This principle is called lithium beam impact excitation spectroscopy (Li-IXS) or lithium beam emission spectroscopy (Li-BES).

With LB diagnostics one can probe the SOL and the pedestal of fusion plasmas, where n_e densities are not too high. In the dense plasma regions the beam is strongly attenuated due to ionisation of the Li atoms.

3.1 Experimental setup of the LB diagnostic

A sketch of the LB diagnostic setup at ASDEX Upgrade is shown in figure 3.1. From a β -eucryptite emitter (at 50 kV voltage), which is heated with ~ 200 W, Li atoms are extracted by an electrode at 43 kV. This electrode is also used to focus the beam. After the formation, the beam is accelerated by the puller electrode (at -1.5 kV). Its negative voltage prevents secondary electrons from entering the beam formation chamber and damaging the emitter. Behind the puller electrode, deflection plates are placed to adjust the beam. Earlier, these deflection plates were also used to hop the beam away from the lines of sight (LOS) of the optical observation system, which is necessary to measure the background radiation. Nowadays, for this purpose, the beam is chopped by a high voltage MOSFET switch [12].

After passing the deflection plates, the beam is neutralized in a heated sodium (Na)

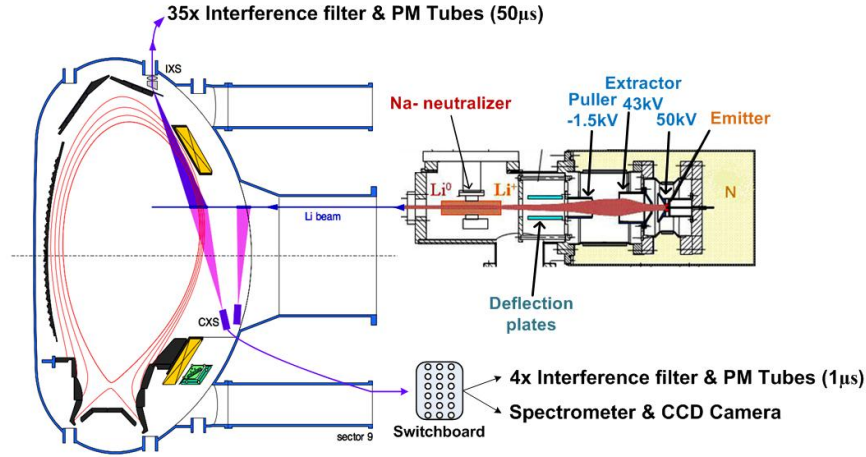


Figure 3.1: Setup of the lithium beam diagnostic at ASDEX Upgrade including the old optical observation systems; Figure taken from [12].

cell. The neutralisation happens through charge exchange processes between the Na and the Li atoms. The neutralized beam with a diameter of 10-15 mm is injected from the low field side (LFS) into the plasma. Two optical observation systems (one from the top and one from the bottom) observe the radiation along the beam, especially around the separatrix. As a part of a diagnostic upgrade (see section 3.1.1), a new optical observation system was installed. It is placed in toroidal direction to the beam (c.f. figure 3.2).

3.1.1 LB diagnostic upgrade

The recently installed LB diagnostic upgrade contains three main parts:

1. New beam chopping system:

A high voltage MOSFET switch was implemented to chop the beam via modulation of the emitter voltage [12]. Before, the modulation of the beam was done by deflection plates. In comparison to the old method, the new chopping extends the lifetime of the emitter, because lithium is only extracted during ‘beam-on’ phases. Further, the beam position is more stable, because the deflection plates are only used for positioning and not for moving (hopping) the beam. The MOSFET increases the switch time between ‘off’ and ‘on’ by a factor of 500 to $0.7 \mu\text{s}$.
2. New faster data acquisition system (SIO):

The new data acquisition system ‘serial in and output (SIO)’, which was designed and manufactured by the IPP, was installed [49]. It enables a data sampling rate of 200 kHz, which corresponds to a time resolution of $5 \mu\text{s}$.
3. New optical observation system:

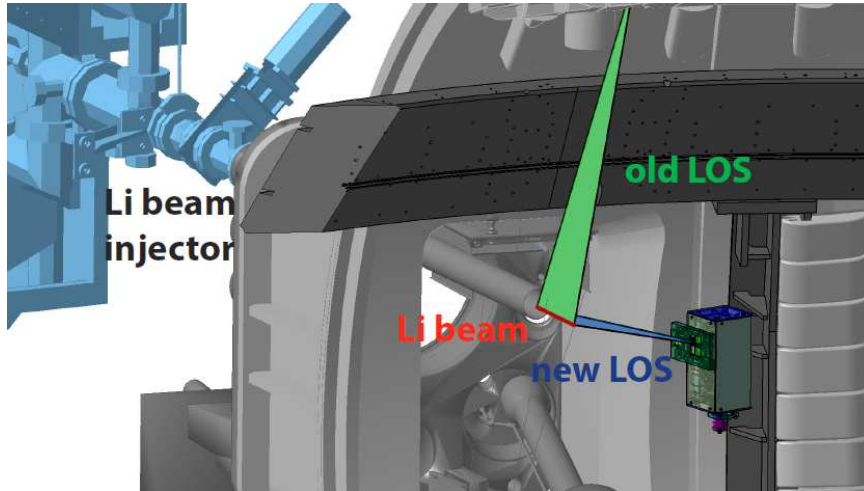


Figure 3.2: New optical observation system and its lines of sight relative to the lithium beam; Figure taken from [13].

The new data acquisition system, which has a better temporal resolution, was installed to make use of the improved photon statistics, delivered by the new optical observation system. It is situated behind the limiter (c.f. figure 3.2) with LOS from the side onto the beam (marked blue in figure 3.2). In comparison to the old observation system (LOS from top down onto the beam, green LOS in figure 3.2), the new optical observation system is much closer to the beam, which increases the photon yield by a factor of 100.

The arrangement of the channels is shown in figure 3.3. Each channel has a dimension of ~ 6 mm parallel and ~ 11 mm perpendicular to the LB. It is elliptically shaped to couple as much light as possible from a rectangular volume along the LB into the $600 \mu\text{m}$ thick circular glass fibres. The channels are arranged in three rows: The middle row consists of 28 channels to cover a wide range along the beam. It is intended for the measurement of electron density profiles. Another two rows, each consisting of 16 channels, are designed to measure poloidal velocities. They are placed one above and one below the middle row. For comparison, four channels of the old optical observation system are plotted red in figure 3.3. These have rectangular cross sections and are larger perpendicular to the beam. ‘Dead’ channels, indicated in blue, have broken fibres and are unusable.

These upgrades of the LB diagnostic give the ability to measure n_e fluctuations [50]. Especially, the high temporal resolution, through better photon statistics and higher sampling rate, is necessary.

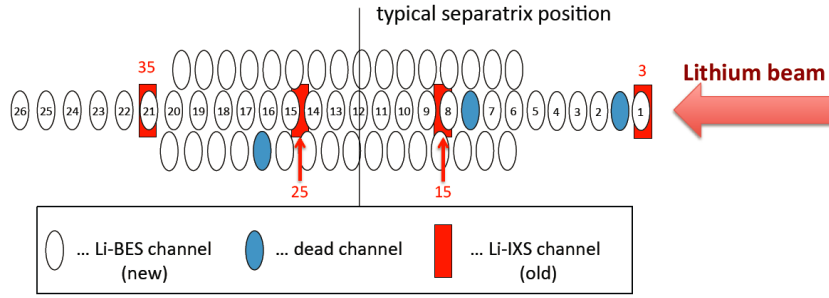


Figure 3.3: Channels of the new optical observation system. For comparison, four channels of the old observation system (called Li-IXS) are indicated in red. Broken (‘dead’) channels are marked blue; Figure taken from [13].

3.2 Lithium beam impact excitation spectroscopy

Li-IXS or Li-BES uses the Li I ($2p \rightarrow 2s$) line radiation profiles to calculate n_e profiles. A collisional radiative model is applied, containing all relevant reactions between plasma particles and the lithium atoms [42]:

- Excitation by collisions with plasma particles
- De-excitation by collisions with plasma particles
- Ionisation
- Charge exchange processes

The relations between these processes and the occupation numbers N_i of the energy states of the lithium atoms are described by a set of coupled differential equations:

$$\frac{dN_i(z)}{dz} = [n_e(z)a_{ij}(T_e(z)) + b_{ij}]N_j(z) \quad (3.1)$$

$$N_i(z = 0) = \delta_{ii}. \quad (3.2)$$

The lithium beam is injected along the coordinate z ($z = 0$ marks the entrance of the beam). The index i denotes the i -th energy level ($i = 1$ stands for Li($2s$), $i = 2$ stands for Li($2p$) and so on). a_{ij} (for $i \neq j$) specifies the rate coefficient for excitation and de-excitation from j to i . Ionisation or excitation to states $i > 8$ (assumed to be equivalent to ionisation) is described by a_{ii} . As these processes happen due to collisions, a_{ij} depends on the temperature $T_e(z)$ (energy) of the plasma particles and the rate is proportional to the particle density $n_e(z)$ at a certain position z , assuming an impurity free plasma, where the electron density is equivalent to the ion density ($n_e = n_p$). Plasma impurities are taken into account by the effective charge number

Z_{eff} , which modifies a_{ij} . The rate coefficients for all types of collisions have been calculated, measured and validated in [45, 51]. Spontaneous emission processes are included by the Einstein coefficients b_{ij} , calculated from transition probabilities of excited lithium atoms [52]. Equation 3.2 gives the boundary condition, that all lithium atoms are in their ground state, when entering the plasma.

The Li-IXS method uses the dependency of the occupation number N_i on the electron density $n_e(z)$. The occupation number itself is linearly proportional to the emitted line radiation:

$$N_2(z) = \alpha \cdot I_{\text{Li } (2p \rightarrow 2s)}; \alpha = \text{const.} \quad (3.3)$$

The diagnostic method uses the most intense transition of Li: Li I (2p \rightarrow 2s). Its intensity $I_{\text{Li } (2p \rightarrow 2s)}$ is connected to the corresponding occupation number of the Li(2p) state (N_2) via the proportionality constant α .

To recalculate the electron density from the measured line radiation profile, one can integrate equation 3.1 stepwise, starting at $z = 0$, as done in [42], or choose a probabilistic data analysis approach [47], which is nowadays mainly used at the LB diagnostic at ASDEX Upgrade. The probabilistic method solves equation 3.1 for varied, cubic spline parametrized n_e profiles. The resulting Li I (2p \rightarrow 2s) line radiation profile is compared with the measured radiation profile. Using bayesian probability theory (BPT) the best match between measured and calculated profile is found. BPT allows to apply physical and prior knowledge about parameters. To generate smooth density profiles, weak constraints on monotonicity of the density profiles are included by priors. A detailed description of the method is given in reference [47].

Chapter 4

Sensitivity Study

The aim of this study is to quantify the sensitivity of the LB diagnostic on n_e perturbations and to determine a parameter range, in which the information about n_e fluctuations is reliable. Several parameters including position, amplitude and width of n_e perturbations are investigated.

4.1 Method

The simulations of the LB diagnostic are organized as follows:

1. Creation of an artificial background n_e profile
2. Addition of a n_e perturbation, varying its position, amplitude and width.
3. Calculation of the occupation number of the Li(2p) state along the n_e profile with and without perturbation.
4. Analysis of the Li(2p) occupation number profiles and comparison with the input n_e profiles.

To simulate the occupation of excited Li states, several existing computer programs have been utilized and extended. A Fortran program called ‘simula’ [42] calculates the occupation numbers of Li for a given artificial n_e profile, solving the set of coupled differential equations given in equation 3.1. The rate coefficients depend on the energy of the Li atoms, therefore, a beam energy of 40 keV is assumed. As introduced in equation 3.3 the occupation number is linearly proportional to the radiation intensity of the Li I (2p \rightarrow 2s) line. Therefore, the occupation number of the Li(2p) state is analysed. In the following, Li_{2p} denotes the occupation number of the Li(2p) state.

4.1.1 Generation of artificial electron density profiles

The background n_e profile, used for the simulations is parametrized by:

$$n_e(z) = \frac{n_{e,max} - n_{e,min}}{2} \cdot [\tanh(\alpha \cdot (z - z_0)) + 1] + n_{e,min} \quad (4.1)$$

The electron density $n_e(z)$ at a certain position z along the beam axis is described by a hyperbolic tangent $\tanh(z)$ [15, 53]. $n_{e,min}$ describes the n_e in the SOL and $n_{e,max}$ stands for the n_e at the pedestal top (c.f. figure 4.1). α indicates the slope of the gradient. It is set to 0.75, which is typical for an L-mode density profile. The positioning of the gradient is done by the parameter z_0 and the +1 after the tanh sets profile to positive values of density.

To create a stronger decay at the profile edge, an additional term $(1 - e^{-\frac{z}{2}})$, which is multiplied with $n_{e,min}$, is introduced:

$$n_e(z) = \frac{n_{e,max} - n_{e,min}}{2} \cdot [\tanh(\alpha \cdot (z - z_0)) + 1] + n_{e,min}(1 - e^{-\frac{z}{2}}) \quad (4.2)$$

The decay close to the entrance of the LB corresponds to the density decrease in real n_e profiles, which is caused by the limiter next to the entrance of the beam. A density profile generated by equation 4.2 is plotted in figure 4.1 in the top graph. The corresponding Li_{2p} profile is plotted at the bottom. The beam axis positions ‘in front’ and ‘behind’ the maximum of the Li_{2p} profile are indicated. In the following, these terms will be used to analyse the positional dependence of the LB diagnostic characteristics to n_e perturbations.

4.1.2 Shaping of electron density perturbations

To investigate the influence of n_e perturbations on the Li I ($2p \rightarrow 2s$) line radiation, n_e perturbations are added to the background profiles. Their shape is assumed to follow a Gaussian distribution $g(z)$,

$$g(z) = \delta n \cdot e^{-\frac{1}{2}\left(\frac{z-\mu}{\sigma}\right)^2} \quad (4.3)$$

with variable height δn , width σ and position μ . δn is proportionately calculated from the background density profile at position $z = \mu$. E.g. in figure 4.2 a perturbation with δn of $1.2 \cdot n_e(4 \text{ cm})$ (black dashed curve) is added to the background n_e profile (black curve). The calculated corresponding Li_{2p} profile is plotted in red (solid: original profile, dashed: profile with perturbation).

The width of the perturbation σ is 0.75 cm, which is corresponding to a FWHM of 1.76 cm. For a Gaussian distribution the FWHM is calculated by

$$\text{FWHM} = 2\sqrt{2 \ln 2} \cdot \sigma, \quad (4.4)$$

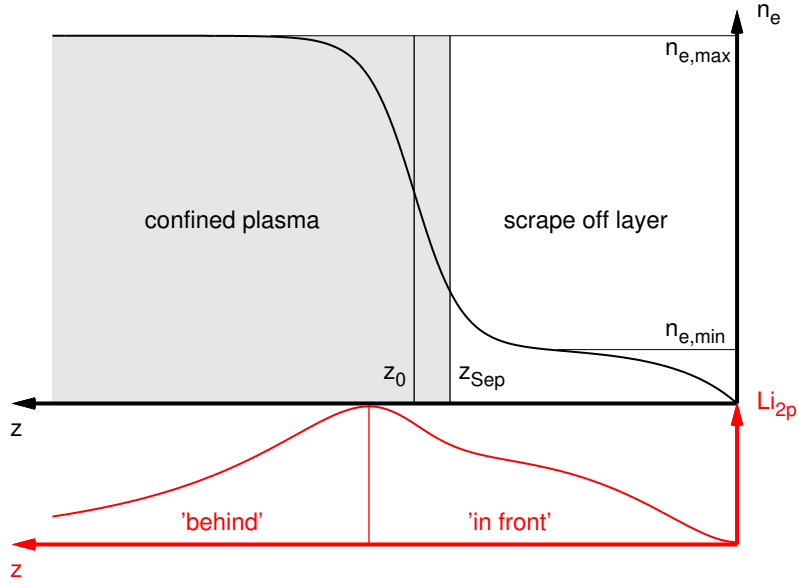


Figure 4.1: Typical artificial n_e profile (black); z_0 , $n_{e,min}$ and $n_{e,max}$ indicate the parameters from equation 4.1. z_{Sep} is a typical position of the separatrix. The corresponding Li_{2p} profile is plotted below (red). The positions 'in front' and 'behind' the maximum of the Li_{2p} profile are marked at the bottom.

or simplified $\sim 2.35 \cdot \sigma$. At the bottom of figure 4.2, the relative deviation of the perturbed profile from the unperturbed profile is plotted. This relative deviation is the difference of the perturbed and the unperturbed profile, which is normalized to the unperturbed profile. Additionally, the FWHM of the perturbation is indicated by horizontal lines. The comparison of the relative deviations (bottom plots) from the n_e and the Li_{2p} shows the reaction of the emission to a n_e perturbation. The relative amplitude of the Li_{2p} is of the order of 0.5, which is smaller than the n_e relative perturbation amplitude of 1.2. The relation between the amplitudes of the emission and density perturbations is investigated in detail in section 4.3. Furthermore, the position of the perturbation maximum in the Li_{2p} is shifted with respect to the position of n_e maximum. Moreover, the whole perturbation is smeared in beam direction owing to the lifetime of the Li(2p) state, which leads to an asymmetric shape of the Li_{2p} perturbation.

4.2 Effects of electron density perturbations on emission profiles

The effects of n_e perturbations on Li I (2p \rightarrow 2s) line radiation profiles are discussed in figure 4.3. An artificial n_e profile, shaped by equation 4.2, is created. Its parameters

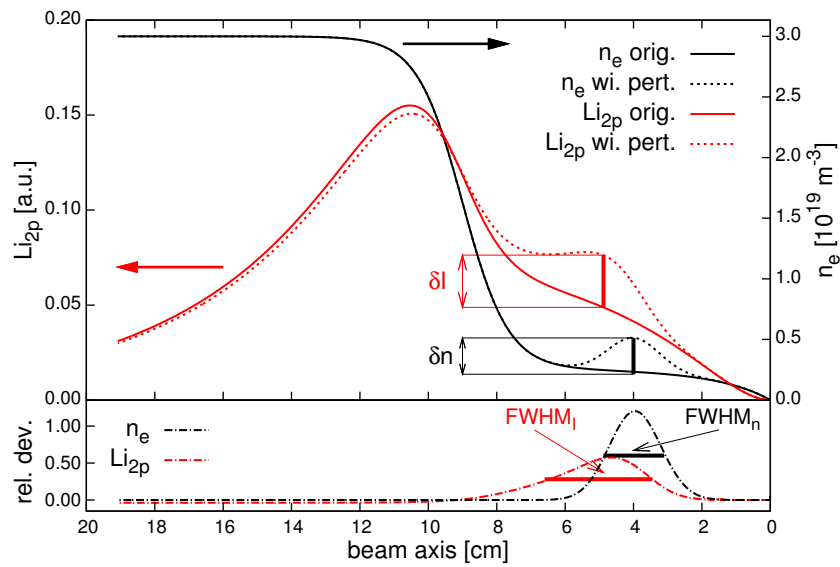


Figure 4.2: n_e and Li_{2p} profile; original profiles are solid lines, profiles with perturbations are dashed. δn and δI are indicated with vertical lines. In the bottom plot the relative deviation (rel. dev.) of the perturbed profile from the unperturbed profile is shown. The FWHM of both curves ($FWHM_I$ for Li_{2p} and $FWHM_n$ for n_e) are marked by horizontal lines.

are: $z_0 = 9$ cm, $n_{e,min} = 2 \cdot 10^{18} \text{ m}^{-3}$ and $n_{e,max} = 3 \cdot 10^{19} \text{ m}^{-3}$. A density perturbation is added to the profile at a position in the SOL ($\mu = 3$ cm, figures 4.3a,b) and at a position in the confined plasma ($\mu = 13$ cm, figures 4.3c,d). Their relative amplitudes $\delta n/n$ are 0.2 (for figures 4.3a,c) and 0.8 (for figures 4.3b,d).

The occupation number of the Li(2p) state depends on its population and de-population. It is populated by de-excitation processes from higher excited atomic states or excitation from the ground state, which is the process of higher importance. De-population occurs, if electrons decay back to the ground state after a certain lifetime or if they are excited to higher states.

In front of its maximum the Li_{2p} profile is dominated by population from the ground state, because all Li atoms of the beam are in their ground state, when the beam enters the plasma (c.f. equation 3.2). Towards the maximum, the de-population of the Li(2p) state by excitation to higher states gets more important. Furthermore, owing to the continuous excitation from the ground state, the occupation of the ground state decreases. Therefore, the probability for population of the Li(2p) state decreases. At the maximum, population and de-population are exactly the same and behind the maximum of the Li_{2p} the depopulation by excitation to higher atomic states or ionisation gets dominant, which leads to a decreasing Li_{2p} profile.

The explained effects essentially influence the reaction of the emission profile to the n_e perturbation. A perturbation situated in the SOL, in front of the Li_{2p} maximum, leads to a positive response in the emission profile (c.f. figure 4.3a,b). There, the dominating process is the excitation from the ground (Li(2s)) to the Li(2p) state. An increase of n_e (induced by the perturbation) leads directly to an increase of the population of the Li(2p) state and therefore, to a positive response in the emission. As discussed in section 4.1.2, the emission signal is smeared and the peak is radially shifted due to the lifetime of the Li(2p) state. Furthermore, one observes that large n_e perturbations in the SOL attenuate the beam, which is expressed by a lower maximum of the Li_{2p} profile (c.f. figure 4.3b and 4.2; red dashed curve). Generalizing, it can be concluded that perturbations in the SOL affect the whole emission profile and lead to a lower Li_{2p} profile at its maximum.

If a perturbation is situated behind the Li_{2p} maximum (4.3c,d), where the de-population of the Li(2p) state dominates, the emission response becomes negative. Here, the n_e perturbation leads to a stronger de-population of the Li(2p) state, which results in a negative response in the emission signal. Moreover, the emission response is non-local and no clear dip can be seen. The non-locality results from a combination of the smearing, which is induced by the lifetime of the Li(2p) state, and the dominating de-population behind the maximum of the Li_{2p} .

In front of the Li_{2p} maximum, the amplitudes of the emission response δI depend directly on the amplitude of the density perturbation δn (larger δn lead to larger δI). Behind the maximum there is a very small inverse dependence of the amplitudes (larger δn leads to larger negative δI), which would not be resolvable in real measure-

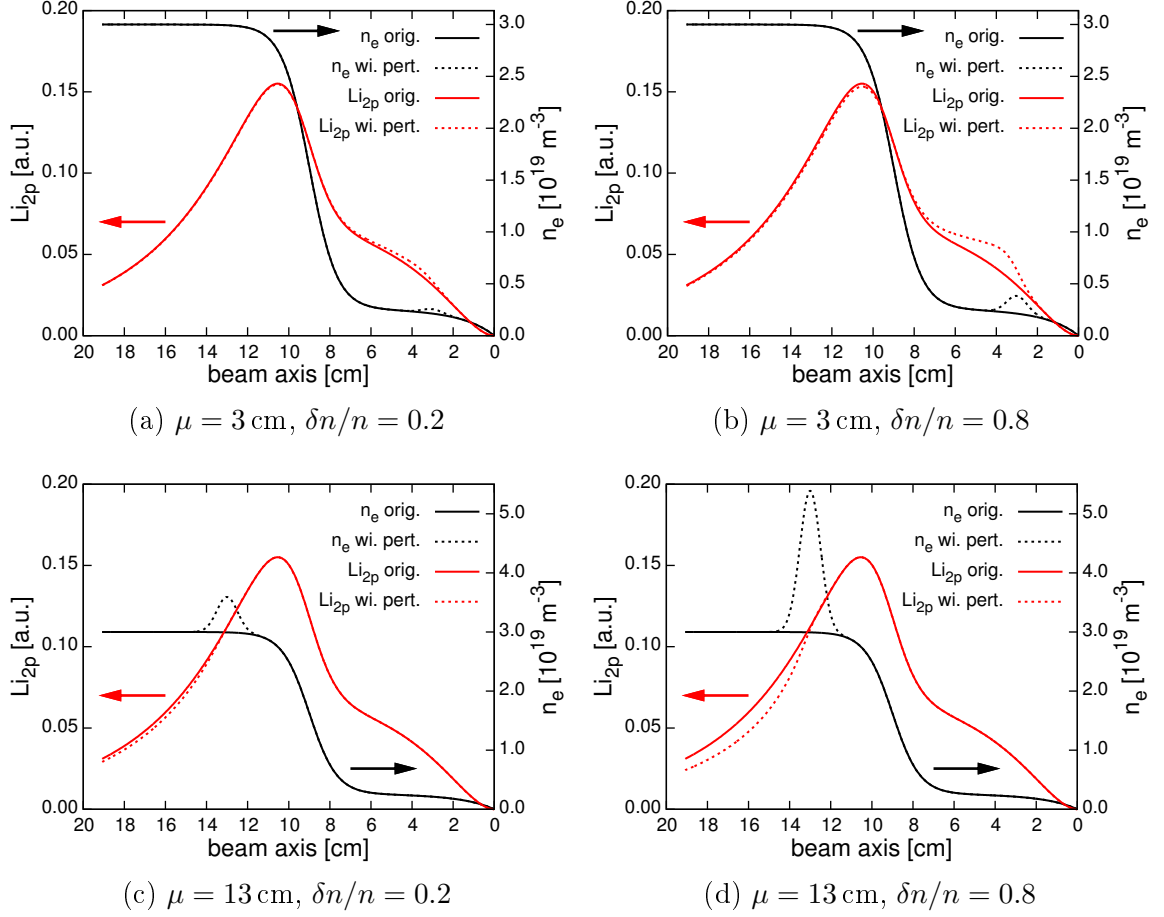


Figure 4.3: n_e and Li_{2p} profiles with perturbations. Original profiles are solid lines, profiles with perturbations are dashed. The artificial n_e profiles are plotted in black, the corresponding emission profiles in red. The emission profile response depends on the position of the electron density perturbation. ‘In front’ (seen in the direction of the beam) of the maximum of the Li_{2p} profile a perturbation leads to a positive δI (a,b). A perturbation situated ‘behind’ the maximum of the Li_{2p} profile generates a negative δI (c,d).

ments. For this reason, only density perturbations in front of the Li_{2p} maximum are investigated in the following sections.

4.3 Emission response on perturbation amplitude

To analyse the profiles, the biggest difference of the Li_{2p} profiles δI is set in relation to the value I of the unperturbed light profile at the beam axis position of δI , leading to the relative emission response $\delta I/I$. The relative amplitude of the n_e perturbation is calculated by $\delta n/n$, where n denotes the unperturbed electron density $n_e(\mu)$ at the perturbation position μ .

A scan through a wide range of $\delta n/n$ at different perturbation positions μ is performed to get detailed information on the relation between relative amplitude of n_e perturbation $\delta n/n$ and relative emission response $\delta I/I$. Its parameters are listed in table 4.1. A typical L-mode profile is used for the background n_e profile (c.f. equation 4.2).

varied parameter	from	to
perturbation position μ	1 cm	11 cm
relative amplitude of the perturbation $\delta n/n$	0.01	1.6
fixed input parameter	value	
width of the perturbation σ	0.5 cm	
scrape off layer electron density $n_{e,min}$	$2 \cdot 10^{18} \text{ m}^{-3}$	
pedestal top electron density $n_{e,max}$	$3 \cdot 10^{19} \text{ m}^{-3}$	

Table 4.1: Amplitude scan parameters

Figure 4.4 shows the results of the scan. $\delta n/n$ is plotted versus $\delta I/I$ and the colour scaling indicates μ . The position of the Li_{2p} maximum is at 10.5 cm.

The following observations can be made:

- Remarkably, there is an almost linear relation between $\delta n/n$ and $\delta I/I$ in the range of $\delta n/n < 1.0$ and $\mu < 10$ cm (c.f. blue, green and yellow curves). For comparison, the black line indicates $\delta n/n = \delta I/I$. There is no 1:1 correspondence between $\delta n/n$ and $\delta I/I$ observed, which is plausible, because of the set of coupled differential equations (see equation 3.1), that are describing the relation between n_e and the Li(2p) occupation number.
- For $\delta n/n > 1.0$ and $\mu \geq 10$ cm non-linearities occur. They are either due to saturation effects, if perturbations are too large, or due to the change of sensitivity, if perturbations are situated too close (in front or behind) the maximum of the unperturbed Li_{2p} profile, which is at 10.5 cm.

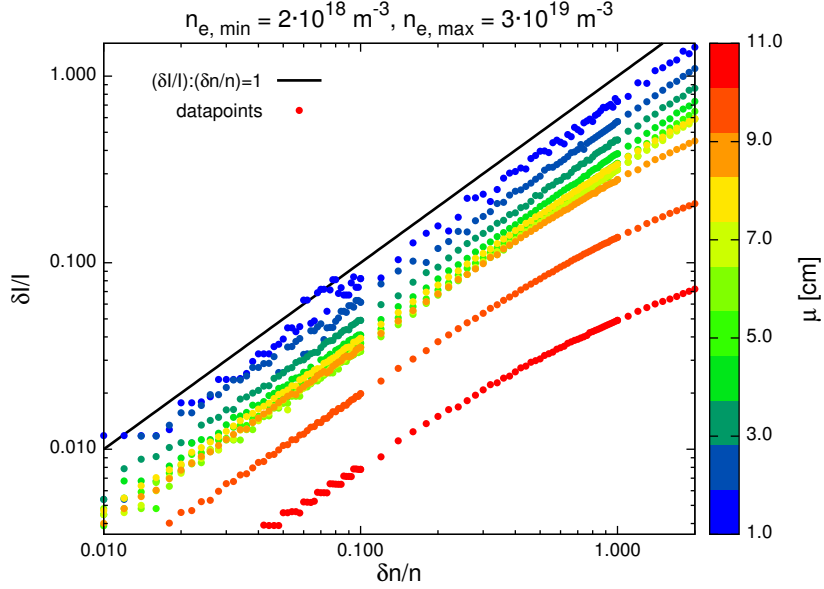


Figure 4.4: Scan with different relative perturbation amplitudes $\delta n/n$ at different positions μ . $\delta I/I$ is the relative emission signal response. The color scaling corresponds to the perturbation position μ . The relation between $\delta n/n$ and $\delta I/I$ is linear in the range of $\delta n/n < 1.0$ and $\mu < 10$ cm.

- As discussed in section 4.2, for a given $\delta n/n$, $\delta I/I$ decreases towards the maximum of the Li_{2p} profile. Therefore, at large μ (red curve) the emission response is much smaller than at small μ . E.g. a perturbation of $\delta n/n = 0.8$ leads to a $\delta I/I$ of 0.13 at $\mu = 10$ cm (red orange curve). The same $\delta n/n$ results in a $\delta I/I$ of 0.4, if the perturbation is situated at $\mu = 2$ cm (light blue curve).

Further simulations with a variation of $n_{e,min}$ lead to consistent results. Although, it has to be considered that a variation of the background n_e profile leads to a change of the Li_{2p} profile, which then changes the sensitivity to n_e perturbations, especially at positions close to the Li_{2p} profile maximum.

One can conclude from these studies, that it is possible to classify the relative amplitude of a n_e perturbation $\delta n/n$ by the emission signal response $\delta I/I$. The influence of the perturbation width is investigated in the following.

4.4 Emission response on perturbation width

To determine radial sizes of blob-filaments from emission profiles, detailed information on the relation between the perturbation width ($FWHM_n$) and the width of the corresponding emission response ($FWHM_I$) is necessary. For this reason, another scan, varying the n_e perturbation width σ , is performed. A summary of the scan parameters

is given in table 4.2.

varied parameter	from	to
perturbation position μ	2 cm	10 cm
relative amplitude of the perturbation $\delta n/n$	0.05	1.00
width of the perturbation σ	0.02 cm	2.00 cm
equivalent FWHM _n	0.05 cm	4.71 cm
fixed input parameter	value	
scrape off layer electron density $n_{e,min}$	$2 \cdot 10^{18} \text{ m}^{-3}$	
pedestal top electron density $n_{e,max}$	$3 \cdot 10^{19} \text{ m}^{-3}$	

Table 4.2: Width scan parameters

The figures 4.5b-f show the dependencies of FWHM_I on FWHM_n and $\delta n/n$ at discrete perturbation positions μ . These positions are indicated by blue vertical lines in figure 4.5a. The colour scaling corresponds to the relative amplitude of the n_e perturbation $\delta n/n$. Red corresponds to a large amplitude, whereas blue indicates a small amplitude. The black dashed lines indicate FWHM_n = FWHM_I. The comparison of the figures 4.5b-f leads to two main observations, concerning the relation between FWHM_n and FWHM_I:

- An independence of $\delta n/n$, excepting $\mu = 10$ cm, where the perturbation is situated close to the maximum of the Li_{2p} profile (c.f. figure 4.5a).
- An almost linear relation between FWHM_n and FWHM_I with changing offset.

The offset of FWHM_I is caused by the smearing, owing to the lifetime of the Li_{2p} state. E.g. figure 4.2 (bottom plot) reveals this effect very clearly. The smearing leads to a broadening of the emission response FWHM_I. Therefore, FWHM_I is larger than FWHM_n. The offset is constant for different $\delta n/n$, owing to the constant smearing at a given beam velocity.

For different perturbation positions μ , different offsets are observed. Because the offset drops towards the maximum of the Li_{2p} profile, a connection between emission profile and FWHM_I could be supposed. As discussed in previous sections (c.f. section 4.2), the effects of n_e perturbations on the Li_{2p} profiles change at the maximum of the Li_{2p} profile from a positive to a negative response. Perturbations situated close to the maximum (c.f. figure 4.5e,f), influence the maximum's position. It is slightly shifted to smaller values along the beam axis. Therefore, the difference of the perturbed and the original profile has a steeper gradient at the decreasing part. This stronger decay lowers FWHM_I. If the perturbation is located at positions $\mu = 2, 4$ and 6 cm, the offset of FWHM_I is constantly ~ 1.5 cm. Whereas, a perturbation situated at $\mu = 8$ cm has an offset of ~ 1 cm and for $\mu = 10$ cm the offset drops to ~ 0.5 cm.

Another effect, which is also induced by the change of emission response at the

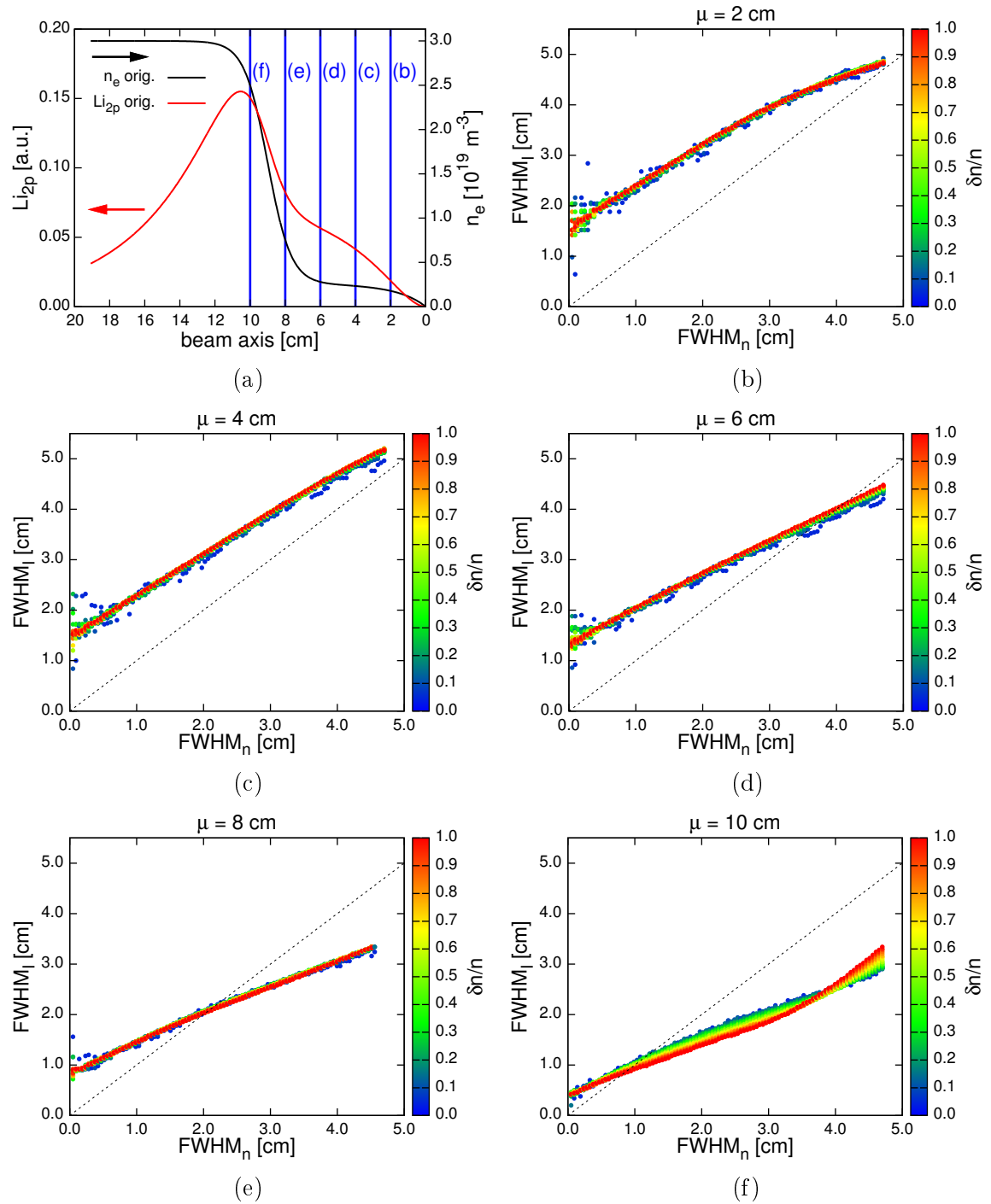


Figure 4.5: Scan of different perturbation widths FWHM_n at several positions μ ; FWHM_I is the emission signal response width. The color scaling corresponds to the relative perturbation amplitude $\delta n/n$. (a) Indication of the density perturbation position μ . The vertical blue lines correspond to different μ in the figures (b-f). FWHM_I shows an offset which is caused by the $\text{Li}(2p)$ lifetime induced smearing.

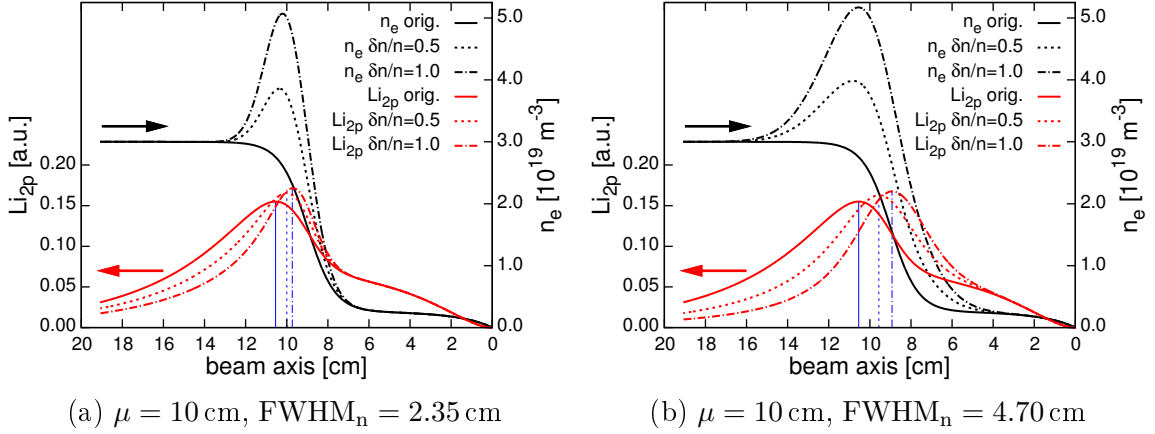


Figure 4.6: n_e and Li_{2p} profiles different perturbation amplitudes $\delta n/n$. The maxima of the Li_{2p} profiles are indicated by blue vertical lines. A larger perturbation width (FWHM_n) leads to a stronger shift of the Li_{2p} maximum.

Li_{2p} maximum, is observed in figure 4.5f. Here, a small dependence of FWHM_I on the relative amplitude of the perturbation $\delta n/n$ is seen, which changes its sign at $\text{FWHM}_n \sim 4$ cm. This effect is explained in detail by figure 4.6. For $\text{FWHM}_n < 4$ cm (c.f. figure 4.6a), an increase of $\delta n/n$ leads to a stronger decay in the decreasing part of the Li_{2p} profile, which lowers FWHM_I . If $\text{FWHM}_n > 4$ cm (c.f. figure 4.6b), the maximum of the Li_{2p} profile gets strongly shifted to smaller values at the beam axis. The shift of the maximum position depends stronger on $\delta n/n$ than at small perturbation widths (c.f. figure 4.6). The reason for this is that at small perturbation width, only the gradient of the n_e profile is changed (c.f. figure 4.6a, black curves). Large perturbation widths lead to a shift of the gradient's position (c.f. figure 4.6b, black curves), resulting in a broadening of FWHM_I in the direction of the gradient's shift (towards smaller beam axis positions) for increasing $\delta n/n$.

Summarizing, the following conclusions can be drawn from the performed sensitivity study:

1. The sensitivity of the LB diagnostic to n_e perturbations decreases towards the maximum of the Li_{2p} profile.
2. The emission signal response amplitude $\delta I/I$ depends linearly on the relative n_e perturbation amplitude $\delta n/n$ over a wide range of $\delta n/n$ and μ (perturbation position).
3. The emission response width FWHM_I shows a linear dependence on the n_e perturbation width FWHM_n with an offset, which is due to the $Li(2p)$ lifetime induced smearing of the emission profile.

Chapter 5

Richardson-Lucy Deconvolution

In the previous chapters, it was often referred to the smearing of the Li I (2p \rightarrow 2s) line radiation profile, which is induced by the lifetime of the Li(2p) state. This chapter discusses the problem in detail and presents a simple method to remove the smearing from the emission profiles. For this purpose, the Richardson-Lucy algorithm is introduced and adapted to the requirements of the LB diagnostic.

5.1 Li(2p) lifetime induced smearing

Excited atomic states decay after a certain lifetime to a state with lower energy. E.g. the Li I (2p \rightarrow 2s) transition has a lifetime of 27.11 ns. If BES is utilized, the excited atoms travel a certain distance, owing to their kinetic energy, before they de-excite. The mean distance (or decay length) l can be calculated by the following equation:

$$l = \sqrt{\frac{2E_{Beam}}{m}} \cdot \tau. \quad (5.1)$$

The beam energy is represented by E_{Beam} , m refers to the mass of the beam atoms and τ is the lifetime of the excited state. The lifetime τ , which corresponds to a 1/e decay, can also be replaced by the half-life $\tau_{1/2}$, which represents a decay to the half of the original amplitude:

$$\tau_{1/2} = \tau \cdot \ln(2). \quad (5.2)$$

This leads to the ‘half-life decay’ length $l_{1/2}$:

$$l_{1/2} = \sqrt{\frac{2E_{Beam}}{m}} \cdot \tau_{1/2}. \quad (5.3)$$

In table 5.1 the decay lengths are calculated for different beam energies and kinds of beam atoms. Additional to Li atoms, beams consisting of Na atoms and high energetic D atoms (typically used for plasma heating) are considered. Lower beam energies or shorter lifetimes reduce the smearing effect. The decay length of a 30 keV Na beam

line (wavelength [nm])	τ [ns]	$\tau_{1/2}$ [ns]	m [u]	E_{Beam} [keV]	l [cm]	$l_{1/2}$ [cm]
<i>Li I</i> (670.8)	27.11	18.79	6.94	30	2.48	1.72
<i>Li I</i> (670.8)	27.11	18.79	6.94	40	2.87	1.99
<i>Li I</i> (670.8)	27.11	18.79	6.94	50	3.21	2.22
<i>Na I</i> (589.0)	16.23	11.25	22.99	30	0.87	0.56
<i>Na I</i> (589.0)	16.23	11.25	22.99	50	1.05	0.73
<i>D I</i> (656.1)	15.46	10.72	2.01	60	3.72	2.58
<i>D I</i> (656.1)	15.46	10.72	2.01	100	4.80	3.33

Table 5.1: Decay lengths for different beam types and energies

is only about 1/3 of the decay length of a 40 keV Li beam. If a Na beam is used, a higher spatial resolution could be achieved. Therefore, several experiments were already performed at ASDEX Upgrade [54] and an atomic cross section database has been compiled [55].

A simple approach, to achieve a better spatial resolution in the Li I (2p \rightarrow 2s) line radiation profile is to remove the exponential decay from the smearing by applying a Richardson-Lucy algorithm to the line radiation profiles. This deconvolution algorithm increases the spatial accuracy and allows determining the exact positions of n_e perturbations from the deconvolved Li I (2p \rightarrow 2s) line radiation profiles.

5.2 Richardson-Lucy algorithm

Originally, the Richardson-Lucy algorithm [56, 57] was developed for image reconstruction. Images, which have been blurred by a known point spread function (PSF), can be recovered by application of the algorithm. The degradation of an image W by a given PSF S to the blurred image H can be mathematically interpreted as convolution (denoted by $*$):

$$H = W * S. \quad (5.4)$$

The PSF gives the response of an imaging system to a point source. E.g. if a Gaussian distribution is utilized, the blurred image of an originally sharply defined object would get diffuse at the edges. $S_{i,k}$ describes the fraction of light emitted at location i , which is observed at location k .

A method for a stepwise iteration of W is provided by bayesian probability theory (BPT). The following derivation is adapted from [56], using the notation that:

- The subscripted letters, like W_i , refer to a value, which is related to a certain position i .
- Unsubscripted letters indicate the sum over all positions i , e.g. $W = \sum_i W_i$.

This nomenclature is also used for $H = \sum_k H_k$ and $S = \sum_j S_j$.

The problem of deconvolution, formulated by means of BPT, denotes:

$$P(W_i|H_k) = \frac{P(H_k|W_i)P(W_i)}{\sum_j P(H_k|W_j)P(W_j)}. \quad (5.5)$$

$P(W_i|H_k)$ is the conditional probability of an event W_i under the requirement of an event H_k . The unknown probability for an event at W_i , $P(W_i)$, is:

$$P(W_i) = \sum_k P(W_i|H_k)P(H_k). \quad (5.6)$$

Substituting equation 5.5 in equation 5.6, leads to:

$$P(W_i) = \sum_k \frac{P(H_k|W_i)P(W_i)P(H_k)}{\sum_j P(H_k|W_j)P(W_j)}. \quad (5.7)$$

The unknown $P(W_i)$ appears on both sides of equation 5.7. Now, via an estimation of an initial $P^{(1)}(W_i)$, a stepwise iteration of $P^{(r)}(W_i)$ (r refers to the r -th iteration step) is possible:

$$P^{(r+1)}(W_i) = P^{(r)}(W_i) \sum_k \frac{P(H_k|W_i)P(H_k)}{\sum_j P(H_k|W_j)P^{(r)}(W_j)}. \quad (5.8)$$

Replacing $P(W_i) = W_i/W$, $P(H_k) = H_k/H$ and $P(H_k|W_i) = P(S_{i,k}) = S_{i,k}/S$ (using $S = \sum_j S_j$) leads to a simplified notation of equation 5.8:

$$W_i^{(r+1)}/W = (W_i^{(r)}/W) \sum_k \frac{(S_{i,k}/S) \cdot (H_k/H)}{\sum_j (S_{i,k}/S) \cdot (W_j^{(r)}/W)} \quad (5.9)$$

The reconstruction has to be a conservative process, therefore, $H = W$, which results in:

$$W_i^{(r+1)} = W_i^{(r)} \sum_k \frac{S_{i,k}H_k}{\sum_j S_{j,k}W_j^{(r)}}. \quad (5.10)$$

Using Bayes' postulate, the initial value $W_i^{(1)}$ is estimated by:

$$W_i^{(1)} = \sum_k \frac{S_{i,k}H_k}{\sum_j S_{j,k}}. \quad (5.11)$$

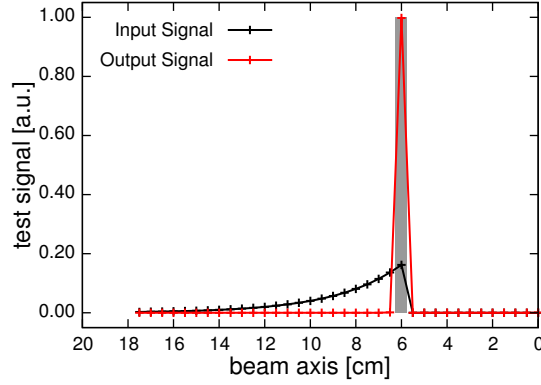


Figure 5.1: Test of the implemented Richardson-Lucy algorithm: A peaked function at 6 cm (grey shaded area) is blurred by an exponential decay (black curve). The blurred data is used as input for the deconvolution algorithm. The reconstructed output is plotted in red. A total recovery of the peak is achieved.

5.2.1 Adaptation and numerical implementation of the algorithm

Equation 5.10 can be iterated numerically. In the frame of this thesis, it was implemented into an Interactive Data Language (IDL) [58] routine, fulfilling the requirements of the LB diagnostic, which were:

- A one-dimensional image, owing to the radially placed LOS of the optical observation system.
- Implementation of the positions of the LOS of the observation system (see section 5.3).
- A correct PSF, which describes the Li(2p) lifetime induced smearing of the Li I ($2p \rightarrow 2s$) line radiation profile.

Expressed in terms of an imaging problem, the PSF $S_{i,k}$ gives the fraction of light originating from location i , which is measured at position k . If only exponential smearing is assumed, the PSF denotes

$$S_{i,k} = \begin{cases} e^{-\frac{x_k - x_i}{l}} & \text{for } x_k \geq x_i \\ 0 & \text{for } x_k < x_i \end{cases} . \quad (5.12)$$

x_i and x_k refer to the positions of the channels i and k along the beam axis. The decay length (c.f. section 5.1, table 5.1) is indicated by l in the denominator of the exponential term. l has to be adapted to the kinetic energy of the LB. Furthermore, $S_{i,k}$ is normalized that $\sum_k S_{i,k} = 1 \forall i$.

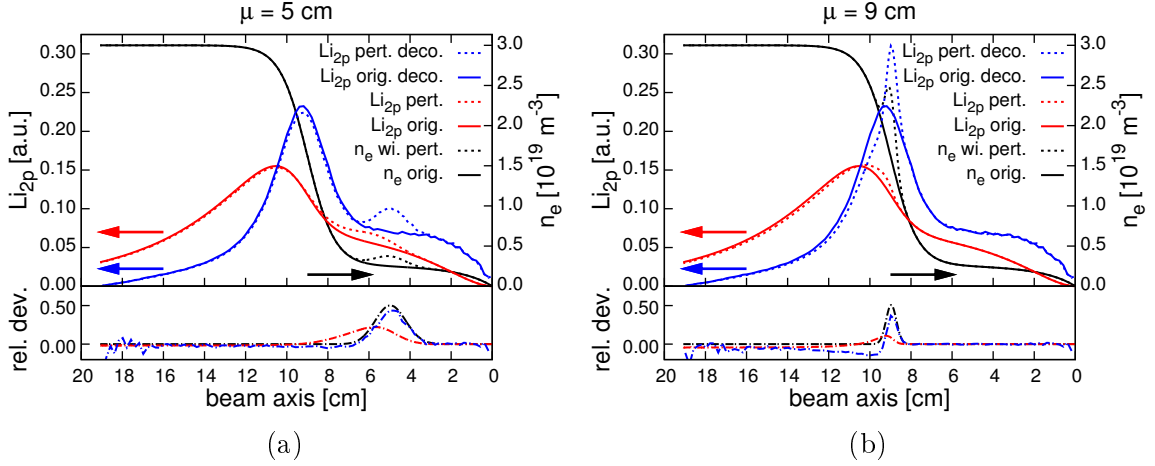


Figure 5.2: Deconvolution of Li_{2p} profiles (in the same representation as in figure 4.2). The n_e profiles (black), the corresponding Li_{2p} profile is calculated (red). Afterwards, the Li_{2p} profile is deconvolved, using the Richardson-Lucy algorithm. The resulting profiles (Li_{2p} deco.) are plotted in blue. The perturbed profiles are indicated by dashed lines. At the bottom of each plot the relative deviation (rel. dev.) of the perturbed profile from the unperturbed (original) profile is plotted. The deconvolved profiles (blue) have almost the same gradients as the n_e profiles.

A numerical test is performed to check the correct implementation of the Richardson-Lucy algorithm (c.f. figure 5.1). A single peaked intensity distribution is set at beam axis position 6 cm. It is smeared by an exponential decay, which is described by the PSF (black curve). On this smeared profile, the deconvolution algorithm is applied. The peak is completely reconstructed in width and amplitude by the method (red curve).

5.2.2 Application on artificial emission profiles

After the successful testing, artificial $Li(2p)$ line radiation profiles are deconvolved by the algorithm. In figure 5.2 two examples are displayed. As explained in chapter 4.2, artificial n_e profiles are generated and density perturbations are added to them. A detailed description of the parameters of the n_e perturbations can also be found in chapter 4.2. The calculated, corresponding emission profiles (Li_{2p} profiles) are used as input profiles for the Richardson-Lucy deconvolution. In figure 5.2a a density perturbation is situated at $\mu = 5$ cm with $FWHM_n = 1.76$ cm and amplitude $\delta n/n = 0.5$. In comparison to the Li_{2p} profiles (red), the deconvolved profiles (blue) show no smearing of the perturbation (c.f. bottom graph). Furthermore, the shape (especially amplitude) and the position of the n_e perturbation are completely recovered by the algorithm.

The effect of beam attenuation caused by the density perturbation, can be observed, comparing the deconvolved profiles with (blue dashed curve) and without (blue solid curve) perturbation around the profile maximum. In the case of the medium sized perturbation in figure 5.2a, the effect is marginal but observable.

In front of the maximum of the deconvolved profiles, the gradients of density (solid black curve) and deconvolved profile (solid blue curve) are almost the same. This suggests that the population of the Li(2p) state (from the ground state) is almost linearly related to n_e .

In terms of resolvability, an extreme example of a density perturbation is presented in figure 5.2b. A rather small perturbation ($\delta n/n = 0.5$, $\text{FWHM}_n = 0.58 \text{ cm}$), situated at the position $\mu = 9 \text{ cm}$, represents almost the limit of resolvability (c.f. chapter 4.4). In the Li_{2p} profiles the perturbed (red dashed curve) and the unperturbed (red solid curve) profiles deviate only marginally from each other. This can also be seen in the bottom graph. Again, the Richardson-Lucy algorithm is able to reconstruct the original perturbation shape from the Li_{2p} profile. In the relative deviation of the deconvolved perturbation from the deconvolved, unperturbed profile (figure 5.2b, bottom plot, blue chain line), an undershoot is observed behind the perturbation, which is due to the change of dominating effects at the Li_{2p} profile maximum from population to de-population (c.f. chapter 4.4). The perturbation is situated that close to the maximum of the Li_{2p} profile, that parts of it are already behind it, leading to a stronger depopulation. The depopulation is not affected by the Li(2p) lifetime but by excitation to higher states. Therefore, it is not removed by the deconvolution algorithm.

To double check the results of the Richardson-Lucy algorithm, the deconvolved (output) profile can be convoluted again with the PSF, which give per definition the Li_{2p} (input) profile. The back-convolution was performed for all deconvolved profiles and show, as obtained, consistency with the original input profiles.

5.3 Implementation of LOS positions

In previous simulations, complete Li_{2p} profiles with a high spatial resolution were analysed. In experimental measurements, the spatial resolution is limited to the LOS of the optical observation system. To adapt the simulations to this requirement, the positions of the LOS from the new optical observation system (see chapter 3.1.1) are implemented. The Li_{2p} profiles are sampled, owing to the positions of the LOS, with a sample interval of 6 mm centred around the nominal LOS position. A sampled profile is plotted in figure 5.3a. The channels are indicated by grey vertical bars. The ‘dead’ (broken) channels (at 5.7 cm and 1.5 cm beam axis position) lead to a loss of information, especially, if a n_e perturbation is located next to the missing channel (c.f. figure 5.3b).

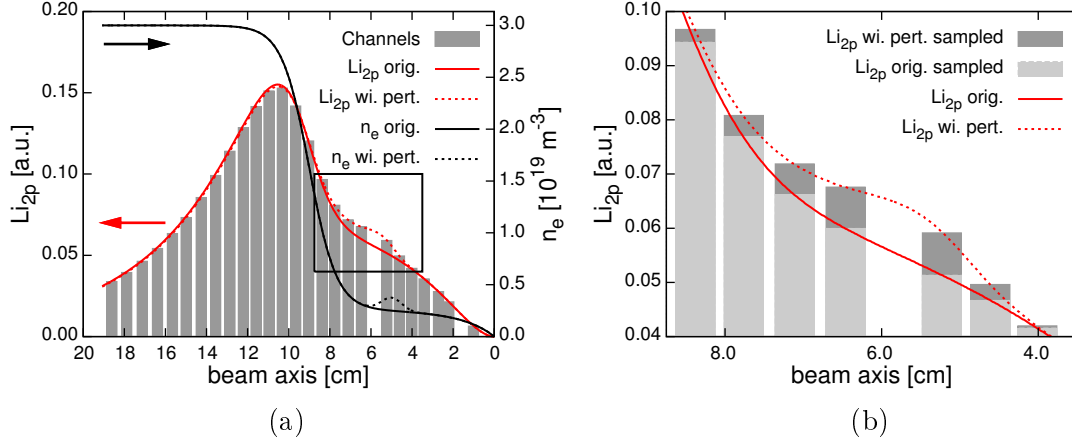


Figure 5.3: Implementation of the channel positions from the new optical observation system (c.f. chapter 3.1.1, figure 3.3). (a) Overview plot, including all channels. (b) Zoom into the black rectangle of figure (a), showing a ‘dead’ channel.

5.3.1 Deconvolution of sampled profiles

The Richardson-Lucy algorithm was developed to run on equidistant grids of pixels, as it is the case in images. Hence, it is necessary to map the positions of the LOS, which are obviously not equidistantly spaced (c.f. figure 5.3), to a regular grid. If the emission profile is smooth, which is the case in the simulations, a different mapping is applicable without causing huge errors. Instead of the original not-equidistantly spaced LOS positions, a regular grid with a width of 0.33 cm, which is about 50% of the distance between two LOS, is used for the new mapping. The emission intensity values, which are measured at the positions of the LOS, are linearly interpolated to the new positions. Afterwards, the Richardson-Lucy deconvolution is applied and then the deconvolved profile is again linearly interpolated on the original positions of the LOS.

The results of this procedure are shown in figure 5.4 for different positions of the density perturbation μ . The perturbation amplitude is set to $\delta n/n = 0.8$ and its width is $\sigma = 0.5$ cm (c.f. equation 4.3), which corresponds to $\text{FWHM}_n = 1.18$ cm. The n_e profiles are plotted in black, corresponding Li_{2p} profiles in red and the deconvolved Li_{2p} profiles in blue. The positions of the LOS of the new observation system are marked by crosses on the profile. In contrast to figure 5.2, one observes in every sub figure that the first value of the deconvolved profile is significantly larger. Because the position of the first channel is at 1.0 cm and not at 0.0 cm as in figure 5.2, the deconvolution algorithm assigns light intensity, which actually originates from positions smaller than 1.0 cm, to the position of the first LOS.

The recoverability of the perturbation shape in the deconvolved profile depends on

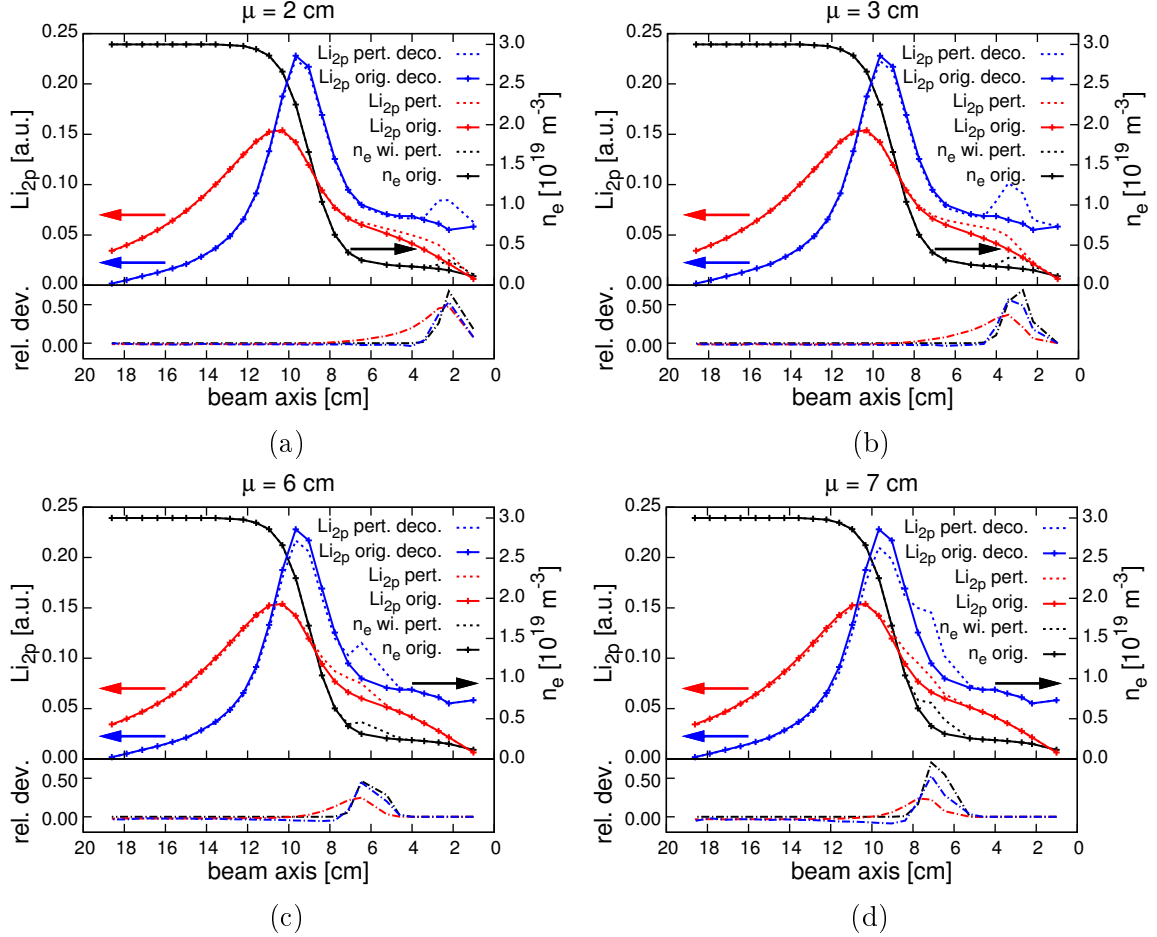


Figure 5.4: Deconvolution of sampled profiles (in the same representation as figure 5.2): The crosses indicate the positions of the LOS of the new observation system. The n_e profiles are black and the corresponding Li_{2p} profiles are indicated in red. The Li_{2p} profiles are sampled and afterwards deconvolved by the Richardson-Lucy algorithm. The resulting profiles (Li_{2p} deco.) are plotted in blue. The resolvability of the perturbation shape is influenced by the perturbation position μ .

the perturbation position, according to the positions of the LOS. E.g. a perturbation situated at $\mu = 2$ cm (figure 5.4a, bottom graph) is totally recovered in its shape, whereas a perturbation at $\mu = 7$ cm shows a deviation, comparing the relative deviations (of the perturbed profiles from the unperturbed profiles) from density and deconvolved profiles at the maximal amplitude (figure 5.4d, bottom graph).

Whether the maximal amplitude is completely resolved or not, depends again on the perturbation position. If the perturbation is situated close to a broken channel, e.g. figure 5.4c, the maximum value of $\delta n/n = 0.8$ is not resolvable, only a value of 0.5 is reached in the input n_e profile and the deconvolved profile (c.f. black and blue curve in the bottom graph). In the figures 5.4a,b,5.4d the maxima of the perturbations are situated closer to the LOS positions, but not exactly at them, which leads to values around 0.7.

In summary, the following points have been achieved:

1. The Richardson-Lucy algorithm was implemented successfully in an IDL routine.
2. On grids with a high spatial resolution, i.e. enough sampling points, the algorithm is able to reconstruct the shape of n_e perturbations from the corresponding Li_{2p} profiles (c.f. figure 5.2) for perturbation positions in front of the Li_{2p} profile maximum.
3. Sampled Li_{2p} profiles, can be reconstructed, via interpolation of the positions of the LOS to a regular grid (c.f. figure 5.4).

The interpolation between the grids assumes a smooth emission profile. This is only the case, if the photon statistics are good and therefore, the emission profile is smooth and not blurred by noise. Measured profiles, sampled with 200 kHz do not fulfil this requirement. Unfortunately, the Richardson-Lucy algorithm gives no possibility to estimate or reduce the noise level. If noise occurs, the algorithm addresses signal, which is originating from noise, to true Li I ($2p \rightarrow 2s$) line radiation from the LB, leading to a wrong, discontinuous deconvolved profile.

For this reason, the deconvolution is not applied to 200 kHz sampled profiles in chapter 6.4. To apply it to these profiles a method to reduce the noise has to be developed. For conditionally sampled profiles (see section 6.2) it is possible to use the algorithm, because the noise is averaged out and smooth emission profiles are provided.

Chapter 6

Blob Size Measurement

In this chapter the data analysis methods, which are introduced in chapter 2.3, are utilized to evaluate the width of blob-filaments.

After a brief introduction of the flux coordinate system (section 6.1), conditionally averaged emission profiles are analysed in section 6.2. Here, a density perturbation is reconstructed from the conditionally averaged emission profile, using an estimated, tanh-shaped, artificial background n_e profile. Furthermore, the conditionally averaged emission profile is deconvolved by the Richardson-Lucy algorithm.

Section 6.3 compares the results of the correlation analysis of measured line radiation profiles and high frequent sampled, evaluated (measured) n_e profiles.

Section 6.4 describes the determination of blob-filament widths, using correlation analysis of measured Li I ($2p \rightarrow 2s$) line radiation profiles. For this purpose, the results from the sensitivity study from chapter 4 are utilized to conclude from the correlation lengths of the line radiation profiles to the actual blob width. Furthermore, the dependence of the blob-filament width on the magnetic field \mathbf{B} (c.f. equation 2.7) is investigated.

6.1 Flux Coordinates

Generally, in axial symmetric toroidal devices the normalized poloidal flux surface coordinate system ρ_{pol} is used as radial coordinate. It enables the comparison of diagnostics, situated at different positions at the torus and is defined as:

$$\rho_{pol} = \sqrt{\frac{\Psi - \Psi_{core}}{\Psi_{sep} - \Psi_{core}}}. \quad (6.1)$$

Ψ denotes the poloidal magnetic flux. It is normalized to the difference of the magnetic flux between separatrix Ψ_{sep} and core Ψ_{core} . Therefore, the coordinate is 0 at the plasma core, increases towards the separatrix to 1 and is larger than 1 in the SOL.

6.2 Perturbation reconstruction using conditional averaging

(The conditionally averaged data, presented in this section, was provided by Tatsuya Kobayashi.)

This section compares a conditionally averaged line radiation profile of discharge #28830 with the mean line radiation profile (background line radiation profile) of the same discharge. In a first approach, a hyperbolic tangent-shaped n_e profile is assumed, whose corresponding line radiation profile fits well to the measured background line radiation profile. The n_e perturbation is reconstructed by variation of a Gaussian shaped perturbation on the tanh-shaped n_e profile (background density profile) till the corresponding, calculated line radiation profile fits to the conditionally averaged line radiation profile. In a further approach, the conditionally averaged and the background line radiation profile are deconvolved, using the Richardson-Lucy algorithm. Finally, the results of both methods are compared.

Chapter 2.3.2 mathematically describes the conditional average. If the chosen reference signal $x(t)$ fulfils a certain condition at time τ_i , all signals ($x(t), y(t), \dots$) are stored in a certain time interval $[\tau_i - \delta t, \tau_i + \delta t]$. Afterwards all sampled intervals are averaged.

The method is applied to the data from the LB diagnostic of discharge #28830 in the interval from 2.5 s to 4 s, using each channel of the new optical observation system (see figure 3.3) as signal. Therefore, a radial, conditionally averaged line radiation profile can be determined. Discharge #28830 is an electron cyclotron resonance heating (ECRH) heated L-mode discharge with a plasma current of 800 kA and a toroidal magnetic field (\mathbf{B}_t) of 2.01 T. The ECRH heating power is 0.3 MW. Figure 6.1a shows the background (mean) line radiation profile for the complete analysed interval (2.5 s to 4 s).

As reference signal, the channel at $\rho_{pol} = 1.04$ is chosen. The condition is that the signal differs more than 2.5 times the standard deviation from the mean value. If the condition is achieved, a time interval of 1 ms is stored at all channels. Each sample of the reference channel is analysed to find the time point with maximum signal amplitude. At this time point, the radial profile over all channels is determined. Afterwards, all profiles are averaged. The resulting profile of this procedure is plotted in figure 6.1b with red solid curves.

To reconstruct the blob-filament, a hyperbolic tangent-shaped n_e profile (see equation 4.1) is assumed as background profile (figure 6.1a, black curve). The hyperbolic tangent is modified by quadric terms in the SOL and in the pedestal top. Furthermore, owing to the limiter, situated next to the LB entrance, the profile is corrected to small densities, for $\rho_{pol} > 1.07$. From the modified profile the corresponding line radiation profile is calculated, which is plotted in figure 6.1a as red dashed curve (fitted Li_{2p}). It shows good agreement with the measured line radiation profile (figure 6.1a, red solid curve). Small deviations are due to the application of a hyperbolic tangent function to

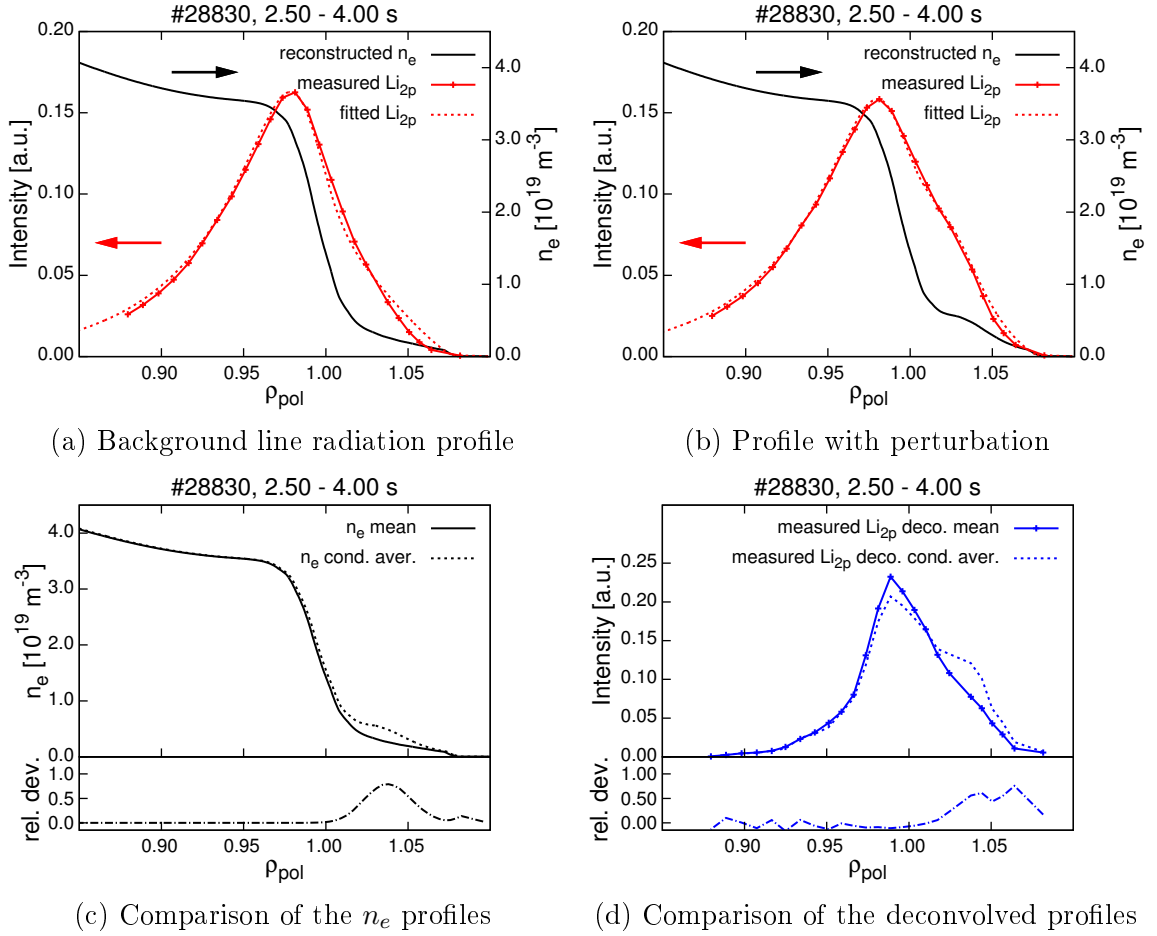


Figure 6.1: Conditionally averaged line radiation profiles. Measured profiles are plotted with red solid curves, the fitted line radiation profiles are indicated by red dashed curves and the corresponding n_e profiles are black. The deconvolved profiles are marked in blue. Figure (a) shows the background line radiation profile including its fit and the to the fit corresponding n_e profile and figure (b) includes the conditionally averaged profile and the associated fits. The background and the conditionally averaged profiles are compared in the figures (c) for the fitted n_e profiles and (d) for the deconvolved profiles. The comparison of the relative deviations, which are calculated from the deconvolved profiles (d, bottom plot) and from the n_e profiles (c, bottom plot), shows agreement in width and amplitude.

describe the density. The agreement of the line radiation profiles is accurate enough to use the modified, tanh-shaped n_e profile as unperturbed background profile. To this background density profile a Gaussian shaped perturbation (c.f. equation 4.3) with variable position μ , amplitude δn and width σ is added. These three parameters are varied, the corresponding line radiation profile is calculated and compared to the conditionally averaged, measured line radiation profile (figure 6.1b, red solid curve), till good agreement of them is achieved (c.f. figure 6.1b, red solid and red dashed curve).

A density perturbation situated at $\mu = 1.035$, with amplitude of $\delta n = 2.25 \cdot 10^{18} \text{ m}^{-3}$ and width of $\sigma = 1.25 \text{ cm}$, which corresponds to a FWHM of 2.94 cm , gives the best agreement. Figure 6.1c compares the perturbed (black dashed curve) and unperturbed (black solid curve) density profiles, from the figures 6.1ab.

Another less complicated possibility to analyse the characteristic parameters of the observed blob-filament directly from the line radiation profiles is the Richardson-Lucy deconvolution, which is introduced in chapter 5. The conditionally averaged, measured line radiation profile and the mean (background) line radiation profile are directly used as input for the deconvolution algorithm. The resulting deconvolved profiles are plotted in figure 6.1d. Comparing the bottom graph (relative deviation of the perturbed profile from the unperturbed (original) profile) of the figures 6.1c and 6.1d, one observes good agreement in position and amplitude. In the deconvolved profile, only one channel at $\rho_{pol} = 1.06$ shows a significantly wrong amplitude, which leads to a too large width. This might be due to a bad interpolation of the data, because there is only the signal from three channels available there. Towards the separatrix (for $\rho_{pol} < 1.05$) the relative deviations show almost the same shape.

From the investigation of the conditionally averaged profiles, the following conclusions can be drawn:

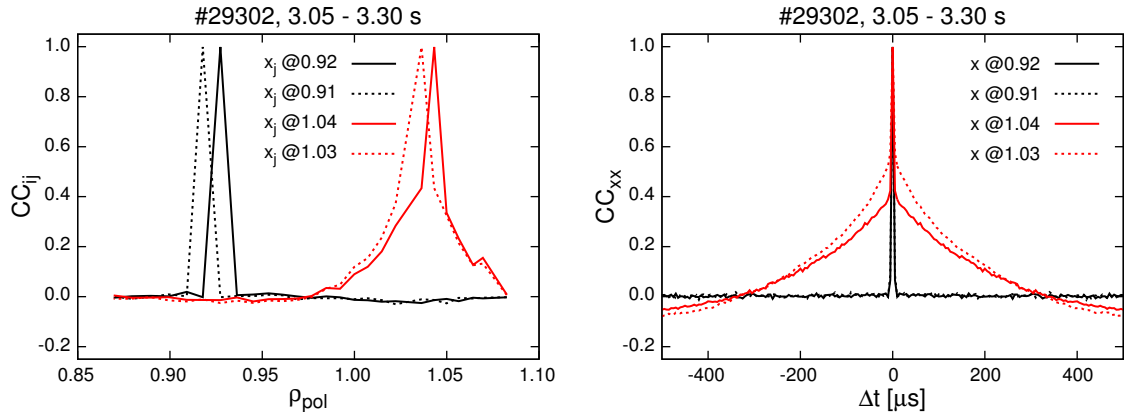
- Blob-filaments can be reconstructed from conditionally averaged, measured line radiation profiles. On a given background n_e profile, a Gaussian shaped density perturbation is varied and the corresponding line radiation profile is compared with the conditionally averaged line radiation profile, till both agree.
- An easier procedure to evaluate position, amplitude and even width, is the Richardson-Lucy deconvolution. With some optimization of the interpolated grid, this tool allows a fast evaluation of blob-filament parameters, directly from conditionally averaged Li I ($2p \rightarrow 2s$) line radiation profiles.

6.3 Correlation analysis of evaluated electron density profiles

For the measurement of turbulent characteristics a high temporal resolution is required. The LB diagnostic is able to sample Li I (2p \rightarrow 2s) line radiation profiles with a rate of 200 kHz. With increasing sample rate, the photon statistic gets worse. Though, there is a poor photon statistic at a sample rate of 200 kHz, the n_e evaluation routine (see chapter 3.2) is able to calculate n_e profiles. These evaluated profiles can be analysed, using the radial cross correlation function CC_{ij} (chapter 2.3.1). In the following, the correlation analyses of the evaluated n_e profiles and of the line radiation profiles are compared by the example of discharge #29302. An L-mode phase 3.05s to 3.30s is investigated. Detailed information on the layout of the discharge is given in section 6.4.1, figure 6.4.

Figure 6.2 displays the radial cross correlation at zero time lag $CC_{ij}(0)$ (for simplicity CC_{ij}) (figure 6.2a,c) and the autocorrelation CC_{xx} (figure 6.2b,d) of Li I (2p \rightarrow 2s) line radiation and n_e profiles. The n_e profiles are evaluated with a standard set of priors: 0.001 for monotonicity and 0.5 for curvature. As radial coordinate the normalized poloidal flux ρ_{pol} (section 6.1) is utilized. Two reference channels x_j (or x for CC_{xx}) in the confined plasma ($\rho_{pol} = 0.92$ and 0.91 , black curves) and two reference channels in the SOL ($\rho_{pol} = 1.04$ and 1.03 , red curves) are chosen for each figure. The choice of two reference channels, which are close to each other has some reason: If radial correlation is observed, two neighbouring channels should observe a similar shape of the correlation function, excluding the ‘noise peak’.

The correlation functions of the Li I (2p \rightarrow 2s) line radiation are shown in figure 6.2a and 6.2b. Owing to the high noise, CC_{ij} and CC_{xx} show strong peaks at x_j . The formation of these peaks is discussed in detail in chapter 2.3.1. In the SOL CC_{ij} shows a wide radial correlation for both positions of x_j (figure 6.2a, red curves), whereas in the confined plasma (black) no correlation between x_j and its neighbouring channels is observed. The CC_{xx} shows temporal correlation in the SOL (figure 6.2a, red curves), which means that blob-filaments have a finite lifetime. These results agree with the results of the sensitivity study, which is performed in chapter 4. The main point of the sensitivity study is that the LB diagnostic can resolve fluctuations in the SOL, but not behind the emission maximum of the Li I (2p \rightarrow 2s) line radiation profile. In the case of this discharge, the central reference channels (figure 6.2, black curves) are situated behind the emission maximum. Here, the noise obscures the correlation, which originates from the beam attenuation. This effect is also discussed in section 6.4.3 (figure 6.8). A high noise level leads to a decrease of the correlation behind the maximum, because the correlation function is normalized to the standard derivation of the signal. If high noise levels occur, the standard derivation is dominated by noise, which then leads to a normalization of the correlation function to the noise amplitude. Therefore, higher noise levels lead to a decrease of the correlation function. Another observable effect is, that owing to the lifetime of the Li(2p) state, the line radiation



(a) Cross correlation of Li I (2p → 2s) profile (b) Autocorrelation of Li I (2p → 2s) profile

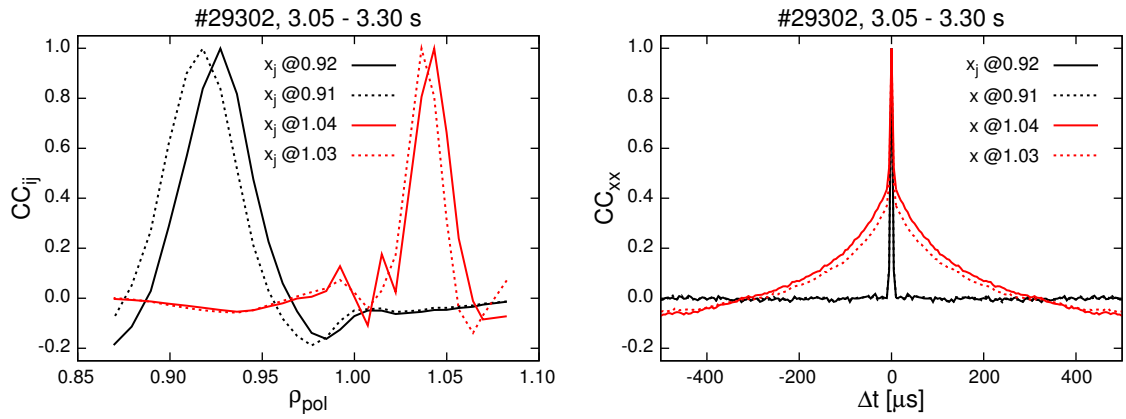
(c) Cross correlation of standard n_e profiles (d) Autocorrelation of standard n_e profiles

Figure 6.2: Comparison of the cross (CC_{ij}) and autocorrelation (CC_{xx}) of Li I (2p → 2s) (a, b) and n_e (c, d) profiles. In each figure four reference channels x_j are chosen, two in the SOL (red) and two in the confined plasma (black). The set of prior parameters in the n_e evaluation routine for (c, d) were: 0.001 for monotonicity and 0.5 for curvature (standard set).

profile gets smeared in the direction of the beam, leading to an asymmetric CC_{ij} . This can be seen, if x_j is situated in the SOL (figure 6.2a, red curves).

The analysis of the evaluated n_e profiles leads to similar results, without the occurrence of asymmetric structures and smearing, because all effects of the line radiation are included in the applied radiative model. The CC_{xx} function of the n_e profile, plotted in figure 6.2d, shows the same behaviour as the CC_{xx} of the line radiation profiles. Thus, the evaluation of autocorrelation times from the evaluated n_e profiles is possible. The CC_{ij} is shown in figure 6.2c. For reference channels in the SOL (red) undershoots to negative values of the CC_{ij} (anti-correlation) next to the peaks are found. Reference channels in the confined plasma (black) observe radial correlation. It is important to mention that the correlation gives no information on the signal amplitude, which is rather low behind the emission maximum of the line radiation profile. The observed radial correlation behind the line radiation profile maximum is not necessarily caused by an actual n_e perturbation, situated at this location. Such a correlation can be generated by a perturbation in the SOL, which attenuates the beam and therefore, reduces the line radiation at all positions further inside the plasma (c.f. section 6.4.3). For this reason the correlation lengths, which are measured behind the maximum of the line radiation profile are not further investigated.

Possible influences of different prior values on the correlation analysis are investigated in figure 6.3. It uses the same plot layout and reference channels as in figure 6.2. In the figures 6.3a and 6.3b all priors are turned off. If a strong prior on the monotonicity and no prior on the curvature is set (figures 6.3c and 6.3d), the distribution of the CC_{ij} is similar to the CC_{ij} of the standard parameter set (figures 6.2c and 6.2d). Again, undershoots of the CC_{ij} function are observed in the SOL.

The evaluated correlation lengths (FWHM of the ‘noise peak’ removed correlation function; c.f. chapter 2.3.1) are listed in table 6.1. For different sets of priors, the

	prior monotonicity	prior curvature	position $x_j = 1.03$	position $x_j = 1.04$
evaluated n_e	0.001	0.5	1.6 cm	2.4 cm
evaluated n_e	off	off	1.2 cm	1.9 cm
evaluated n_e	0.1	off	1.4 cm	2.2 cm
line radiation			3.5 cm	3.8 cm
corresponding n_e perturbation			2.0 cm	2.4 cm

Table 6.1: Correlation lengths (FWHM) measured in the SOL

deviation between the observed correlation lengths is rather small, which confirms the independence of the correlation analysis of the prior set. The correlation lengths from the line radiation profiles are significantly larger than the correlation lengths from the evaluated n_e profiles. This is due to the previously discussed Li(2p) lifetime induced smearing of the line radiation profile. To evaluate the size of the corresponding density

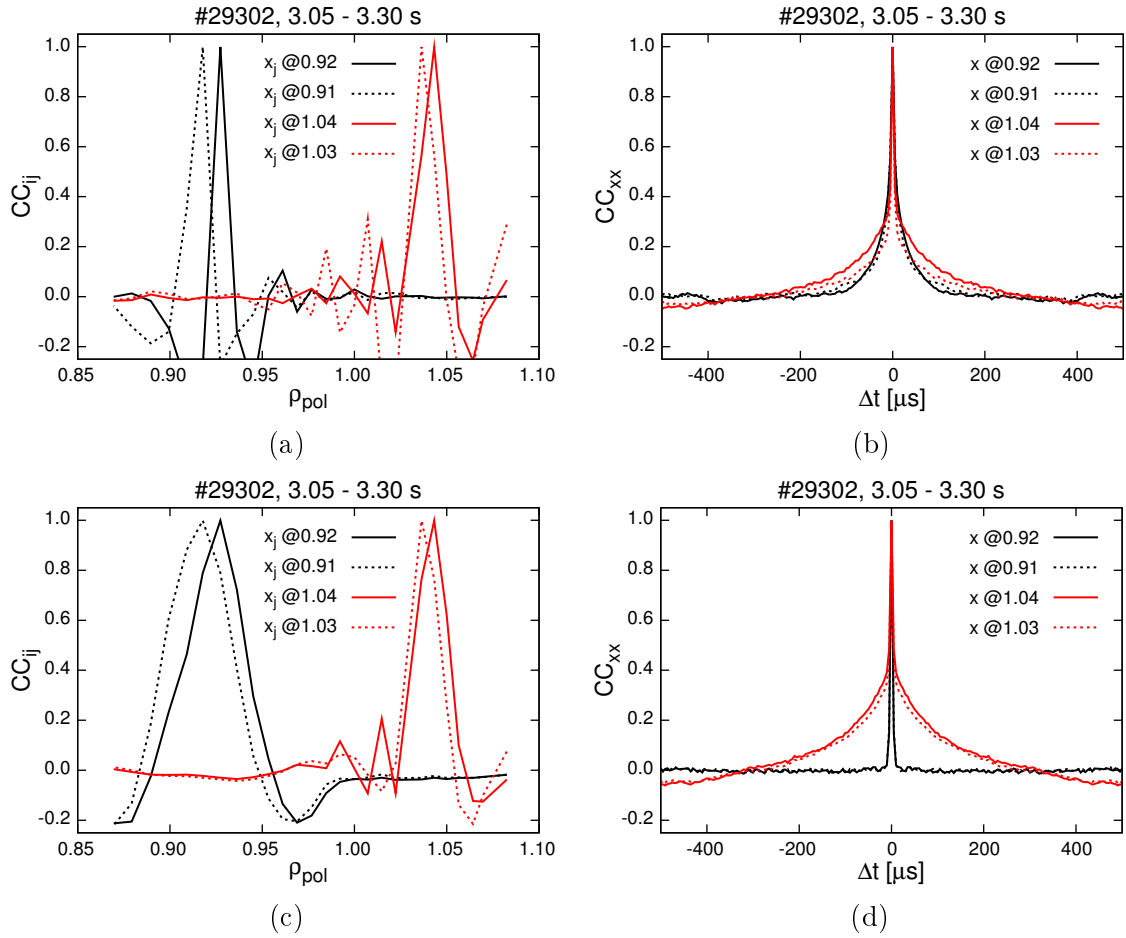


Figure 6.3: Cross CC_{ij} and autocorrelation CC_{xx} of n_e profiles for different prior values: (a, b) the priors are switched off, (c,d) the monotonicity prior is 0.1 (100 times the standard set) and curvature prior is off. In each figure four reference channels x_j are chosen, two in the SOL (red) and two in the confined plasma (black).

perturbation, the relation between n_e perturbation width and perturbation width of the line radiation has to be utilized (c.f. section 6.4.5). The n_e perturbation widths, which are calculated from the line radiation correlation lengths, are in good agreement with the correlation lengths from the n_e profiles (c.f. table 6.1).

Summarizing, one can conclude that the information, gained from correlation analysis of evaluated n_e profiles, gives correlation lengths in the same range as the correlation analysis of the line radiation profiles. To determine the width of blob-filaments directly from the line radiation profiles, the relation between emission profile width and n_e perturbation width (see chapter 4.4) has to be used. Furthermore, the exact relation for a certain discharge can be gained, using an averaged, evaluated n_e density profile as input density profile in the simulations.

6.4 Blob size determination by correlation analysis

In the following, the procedure to measure blob-filament sizes, using correlation analysis of Li I ($2p \rightarrow 2s$) line radiation profiles, is described. To investigate the dependency of the blob size on the magnetic field (equation 2.7), a series of discharges with varying \mathbf{B}_t is performed (see section 6.4.1). An example of a temporally resolved propagating filament is given in section 6.4.2, to show that the observed structures match to the definition of blob-filaments.

To find the relation between the width of the emission profile perturbation and the blob size, the simulations performed in chapter 4.4 are repeated, using the evaluated n_e profile, as input density profile (see section 6.4.3 and 6.4.5). Furthermore, the influences of noise and varying density perturbation amplitude on the correlation analysis method is evaluated in section 6.4.3. In section 6.4.6, the measured blob sizes are compared with the blob sizes, which are derived from theory.

6.4.1 Discharge layout

The analysed series of discharges is characterized by a layout, which is exactly the same for all discharges, excepting a variation of \mathbf{B}_t . The plasma current I_p of several discharges (c.f. table 6.2) is changed to keep the ratio between toroidal \mathbf{B}_t and poloidal \mathbf{B}_θ magnetic field constant. A summary of the plasma parameters from the performed discharges is given in table 6.2. Additionally, the magnetic connection length L_\parallel , which is another parameter of the most stable blob size δ_* (c.f. chapter 2.1.2), is included in the table. Figure 6.4 shows an overview plot of the plasma parameters. The discharge layout corresponds to a low power discharge with two ohmically heated L-mode phases (light grey shaded), which enclose a neutral beam injection (NBI) induced H-mode phase (3.5 to 5.5 s, dark grey shaded). In figure 6.4b the stored energy in the plasma (W_{MHD} , black curve) and the NBI heating power (P_{NBI} , blue curve) are plotted over the time.

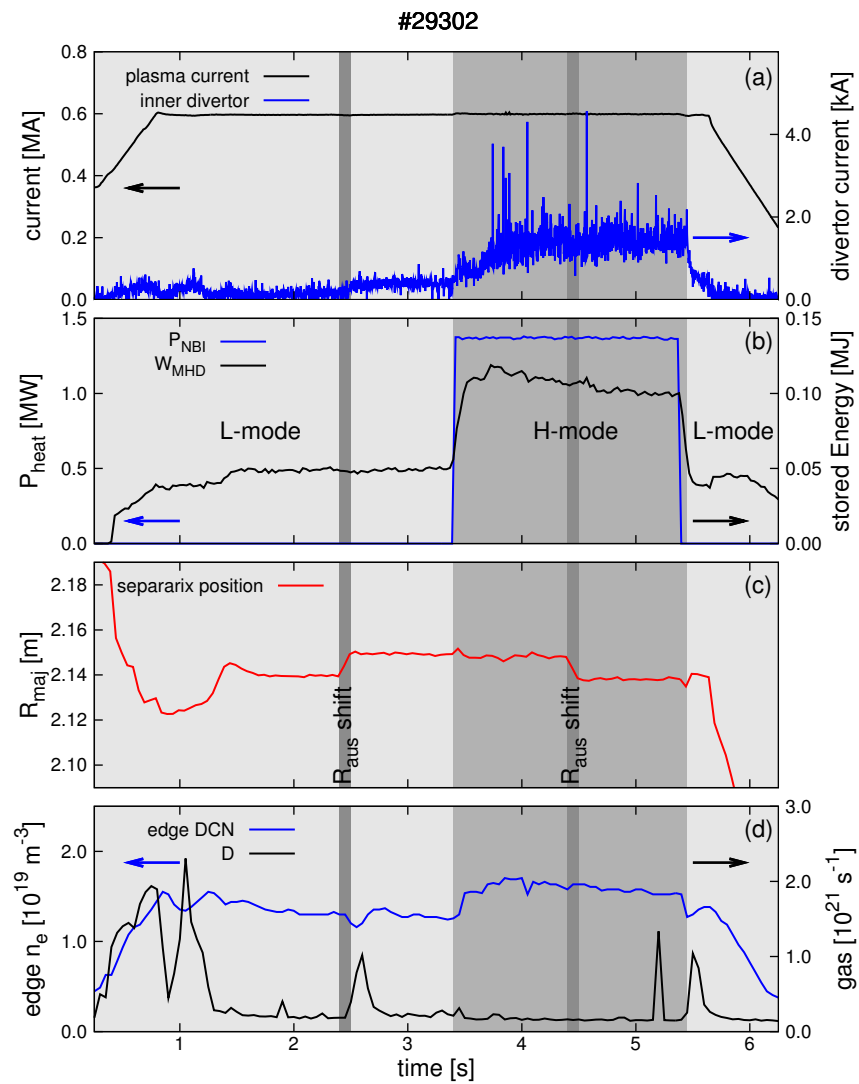


Figure 6.4: Overview plot of the parameters from discharge #29302.

number	toroidal magnetic field \mathbf{B}_t [T]	plasma current I_p [MA]	magnetic connection length L_{\parallel} at $\rho_{pol} = 1.02$ and $t = 3.15$ s [m]
#29302	2.5	0.60	18.37
#29303	1.8	0.60	20.98
#29306	1.4	0.60	17.00
#29307	1.4	0.60	17.71
#29308	3.2	0.60	32.47
#29309	2.5	0.83	18.92
#29310	1.4	0.47	24.35
#29311	1.8	0.60	20.22
#29312	1.8	0.60	20.76
#29315	3.2	1.07	17.74

Table 6.2: Analysed discharges and plasma parameters

Furthermore, two ‘ R_{aus} ’ shifts, which move the horizontal position of the plasma, are performed at 2.5 and 4.5 s, to move the plasma in front of different channels of the optical observation system. This should check, if e.g. a poorly calibrated channel, creates artefacts, which then lead to wrong results. In figure 6.4c, the position of the separatrix at the low field side midplane is shown. During the ‘ R_{aus} ’ shifts, indicated dark grey, the separatrix position is changed by about 1 cm.

The gas fuelling is feedback controlled [59], a setting which regulates the amount of fuelling gas to keep the line averaged n_e at the plasma edge, which is measured by deuterium cyanide laser interferometry (DCN), constant. Figure 6.4d includes a curve of the line averaged n_e (edge DCN, blue) and a curve of the fuelling gas rate (D, black). If the density drops, e.g. after the first ‘ R_{aus} ’ shift (at 2.5 s), the fuelling gas valves open and the fuelling gas rate increases, till the edge density recovers (c.f. peak at 2.65 s).

The mean, evaluated n_e profiles of some of the analysed discharges with different \mathbf{B}_t are plotted in figure 6.5. Two different coordinate systems (flux coordinates ρ_{pol} (figure 6.5a) and beam axis coordinates (figure 6.5b)) are utilized. In both, the profiles show agreement within the errorbars in the SOL, excepting discharge #29308, which has an about 50% larger density in the SOL. The agreement of the profiles in the flux coordinate system is important, because the blob sizes are analysed from different discharges at locations with equivalent magnetic flux (see section 6.4.6).

The agreement of the profiles in the beam axis coordinate system is important for the sensitivity of the LB diagnostic to n_e perturbations. In this case the same sensitivity for all analysed discharges is assumed. The deviation of discharge #29308 is neglected in the further procedure and the sensitivity of the LB diagnostic is investigated on a mean evaluated n_e profile from discharge #29302 (c.f. sections 6.4.3,

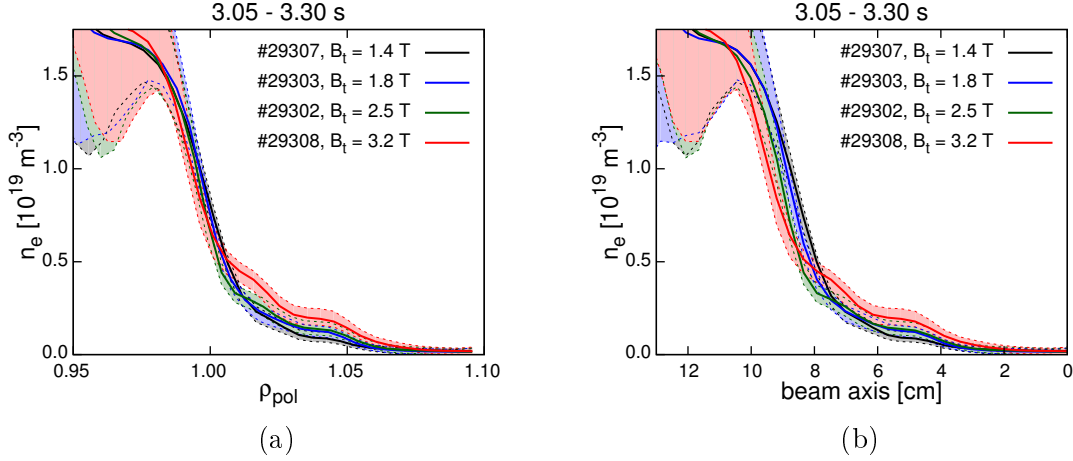


Figure 6.5: Evaluated n_e profiles of some of the analysed discharges (with varying \mathbf{B}_t). The profiles are plotted, using flux surface coordinates ρ_{pol} (a) and using the beam axis coordinate (b). Excepting discharge #29308, all profiles agree within the errorbars, especially between $\rho_{pol} = 1.00$ and 1.05 , where the analysis of the blob sizes is performed (c.f. section 6.4.6).

6.4.5).

For the performed discharge series, the position of the line radiation profile maximum is situated inside the separatrix. This leads to a good sensitivity to n_e perturbations in the SOL (c.f. chapter 4.2), because the resolvability of n_e perturbations is possible if the perturbation position is in front of the line radiation profile maximum.

6.4.2 Spatio-temporal resolution of blob-filaments

The radial cross correlation function $CC_{ij}(\Delta t)$ enables a spatio-temporal resolution of plasma filaments by variation of the time lag Δt , which is the temporal shift between the two analysed signals (see chapter 2.3.1).

Figure 6.6 shows the spatial correlation of the Li I ($2p \rightarrow 2s$) line radiation from discharge #29307 (analysed from 1.75-1.85 s) for different Δt . As reference signal, the channel at $\rho_{pol} \sim 1.05$ is chosen and the colour scaling indicates the value of the CC_{ij} . The reference channel is marked by a vertical black solid line. Here, at $\Delta t = 0 \mu\text{s}$ (indicated by the white cross) occurs the ‘noise peak’. It has been removed by the method, introduced in chapter 2.3.1. Therefore, the correlation function is 0.4 at its maximum and not 1.0 as it is implied by its definition. At $\Delta t = -200 \mu\text{s}$ strong correlation is observed at $\rho_{pol} \sim 1.03$. For larger Δt the maximum of the correlation function moves towards larger radii. At $\Delta t = 200 \mu\text{s}$ the correlation vanishes. The movement towards larger radii is indicated by the black dashed line.

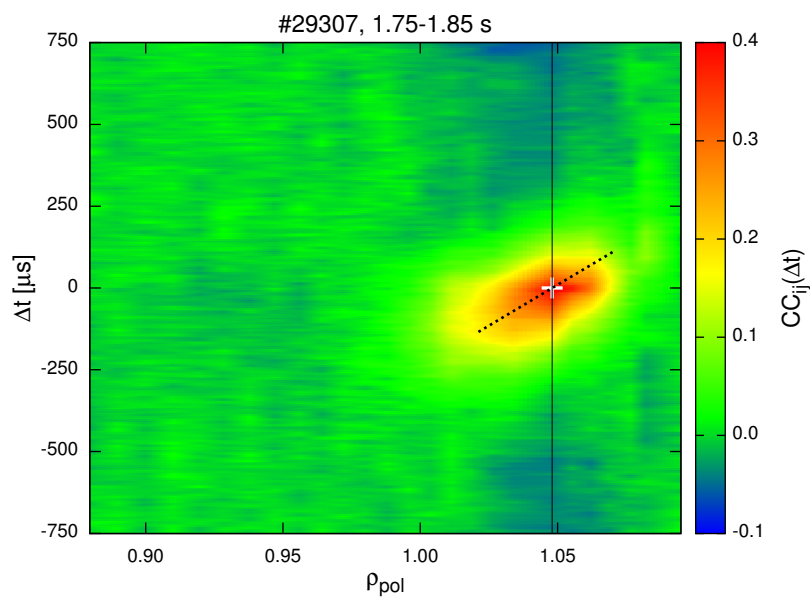


Figure 6.6: Spatio-temporal structure of a blob-filament. The colour scaling gives the value of the spatial cross correlation function $CC_{ij}(\Delta t)$. The time lag Δt is the abscissa in the graph and the radial coordinate is given by the normalized flux coordinate (ρ_{pol}). The reference channel ($\rho_{pol} \sim 1.05$) is indicated by a vertical black line. The white cross marks the position of the removed 'noise peak'. The black dashed line indicates the propagation velocity and direction towards larger radii.

The observed structures fulfil the definition of a blob-filament (c.f. chapter 2.1):

- They have a finite lifetime.
- They are denser than the background density (indicated by higher line radiation radiation) and single peaked.
- They move towards larger radii, which is consistent with the theoretically predicted direction of the blob movement (c.f. chapter 2.1.1).

For this reason, it is admissible to identify the measured structures as blob-filaments.

6.4.3 Simulation of density perturbations on a mean evaluated density profile

There are two important motivations to simulate blob-filaments on the measured evaluated n_e profiles:

1. To test the cross correlation analysis algorithm and to investigate the influence of noise and different perturbation amplitudes.
2. To get the most accurate relation between the width of the emission profile perturbation and the blob size.

For this reason, the temporal behaviour (intermittency) of blob filaments are included in the simulations, which are performed in chapter 4. Furthermore, a measured, evaluated n_e profile is used as input profile for the simulations and random noise is added on the corresponding line radiation profiles.

The performed simulations create time traces, using a mean evaluated n_e profile (discharge #29302, 3.05-3.30 s) as input profile. Intermittent Gaussian shaped density perturbations, which have a random Gaussian distributed amplitude (between -100% and +100% of the input n_e), are added to the mean (input) density profile, which is then sampled to the channel positions of the new observation system (c.f. figure 5.3). The temporal distribution of the perturbations is assumed to be Gaussian shaped and their frequency is set to 2.5 kHz with a lifetime of 400 μ s. In total, a time interval of 50 ms is generated. The radial position of the artificial density perturbation maximum is chosen to be in the SOL, where blob-filaments are observed (c.f. figure 6.9). In section 6.4.6, perturbations are analysed at reference channels situated around $\rho_{pol} \sim 1.02$, which corresponds to beam axis positions from 6.4 cm to 7.1 cm (for discharge #29308, which generally deviates from the other analysed discharges). Since the perturbation position only weakly affects the relation between perturbation width and line radiation profile perturbation width, the radial position of the artificial n_e perturbation is set to 6.4 cm in the beam axis coordinate system. The perturbation width σ is set to 1.75 cm, which corresponds to a FWHM of 4.11 cm.

The corresponding line radiation (Li_{2p}) profiles are calculated for each time step, using the ‘simula’ code (see chapter 4.1). Afterwards, these profiles are also sampled

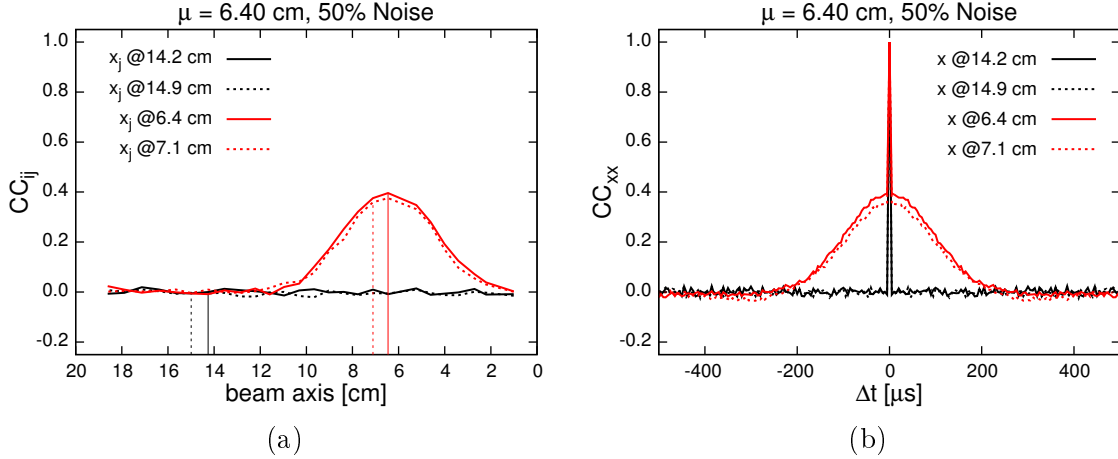


Figure 6.7: Cross CC_{ij} (a) and autocorrelation CC_{xx} (b) of artificial n_e time traces. The positions of the reference channels are indicated by vertical lines. Though, 50% noise is added to the signals, the original shaping of the perturbations is spatially and temporally recovered.

to the channel positions of the new observation system.

To investigate the influence of noise on the analysis methods, random Gaussian distributed noise is added to the density and line radiation time traces. The noise amplitude is determined in terms of percentage from the perturbation amplitude. E.g. 50% noise corresponds to a standard deviation of the noise amplitude, which is 50% of the maximal signal amplitude (the mean noise amplitude is zero). In the following, the density and line radiation profiles are analysed, using the cross correlation function.

Figure 6.7 shows the cross (CC_{ij}) and autocorrelation (CC_{xx}) function of artificial density time traces, which are blurred by 50% noise. Two reference channels at the density perturbation (figure 6.7a, indicated by red vertical lines) and two reference channels away from the density perturbation (figure 6.7a, marked with black vertical lines) are chosen. The reason for the choice of two spatially close reference channels is, that if structures are occurring, both channels should observe the analogue spatial shape of the CC_{ij} .

As discussed in chapter 2.3.1, the additional noise forms the ‘noise peak’, which is observed in the autocorrelation function CC_{xx} at $\Delta t = 0$ s (figure 6.7b). It is removed from the cross correlation CC_{ij} (figure 6.7a), leading to a smooth shape of the correlation profile.

In figure 6.7 the reference channels, which are situated close to the maximum perturbation amplitude (red curves), temporally and spatially resolve the shape of the perturbation, although there is 50% noise on the signal. As expected, the channels, which are situated away from the perturbation (black curves), do not observe anything. For this reason it can be concluded, that the applied analysis method is appropriate.

The analysis of the corresponding line radiation time traces, is shown in figure 6.8. As it is done for the correlation of the density, two reference channels close to the perturbation (red curves) and two channels behind the perturbation (black curves) are chosen. Furthermore, the ‘noise peak’ is removed from the cross correlation.

The figures 6.8a,b include the cross and autocorrelation at a noise level of 2%, which is rather low and not comparable with experimental conditions. It is interesting to study the correlation at low noise level, because here correlation is observed, which will be obscured, if high noise levels are occurring.

At the reference channels (figure 6.8a, black curves), situated behind the maximum of the line radiation profile (indicated by a blue vertical line), one observes correlation. This is owing to the beam attenuation, caused by the density perturbation, which lowers the line radiation profile in its decreasing part (c.f. chapter 4.2). As expected, the reference channels at the perturbation position (figure 6.8a, red curves) resolve a correlation around the density perturbation position and anti-correlation for positions behind the line radiation maximum. The change between correlation and anti-correlation does not occur at the position, where the maximum is indicated (blue vertical line at 11.75 cm), because the position of the unperturbed line radiation profile maximum is marked. A large density perturbation shifts the line radiation profile maximum towards smaller beam axis positions (c.f. chapter 4.4). Therefore, the shift from positive to negative values of the CC_{ij} occurs at 10.5 cm, which is the position of the maximum of the perturbed line radiation profile.

The temporal shape of the initial, artificial perturbation is also recovered by the autocorrelation function (figure 6.8b).

At larger noise levels (see figure 6.8c,d, 50% noise), the previously discussed effects disappear, respectively they are obscured by the large noise amplitudes. There is only a small anti-correlation between positions in front and behind the line radiation profile maximum observable (figure 6.8c, black curves). The actual perturbation is again completely recovered in its temporal and spatial shape.

6.4.4 Comparison with measured data

The simulations are compared with measured data. Figure 6.9 shows the correlation of the line radiation from discharge #29302, analysed from 3.05 to 3.30 s. The cross correlation CC_{ij} (figure 6.9a) has almost the same shape as the CC_{ij} from the artificial line radiation profiles (blurred with 50% noise), plotted in figure 6.8c. In the SOL large blob-filaments are observed. The different amplitude at the maximum of the CC_{ij} (red curves) can be due to different noise levels at the chosen reference channels.

The temporal shape (given by the autocorrelation function CC_{xx} in figure 6.8b) differs from the one, which is assumed in the simulations. The CC_{xx} shows a distribution that is strongly peaked at $\Delta t = 0$ and rather triangularly shaped instead of the Gaussian distribution assumed in the simulations. This is an effect, which can be

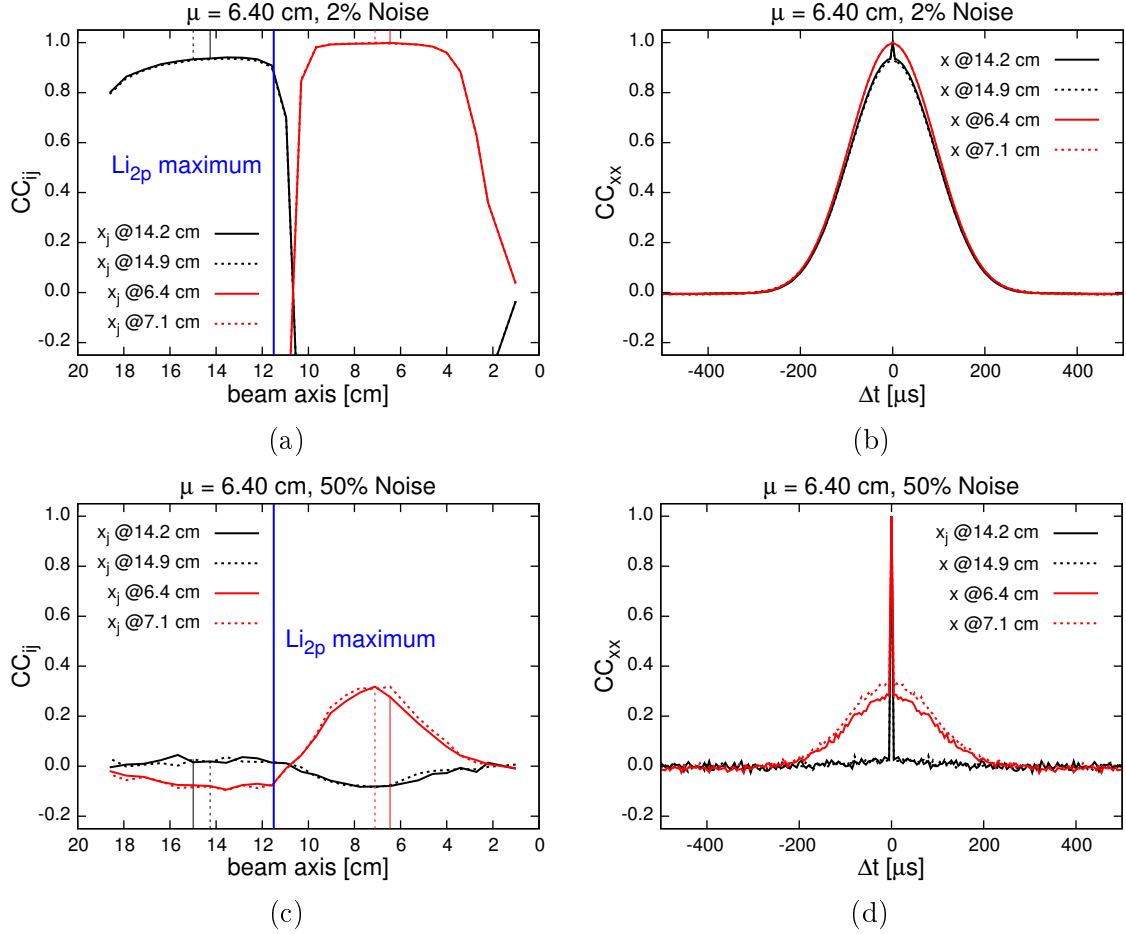


Figure 6.8: Cross (a, c) and autocorrelation (b, d) function of artificial line radiation time traces. Two reference channels are chosen to be at the perturbation position (red curves) and two reference channels are positioned behind the perturbation (seen in beam direction). The position of the maximum of the line radiation (Li_{2p} maximum) is indicated by a vertical blue line. Random noise is added to the input time traces. In (a, b) it is 2% of the maximum perturbation amplitude, in (c, d) it is set to 50%. The high noise in (c, d) obscures the correlation behind the profile maximum, which is observed at a low noise level (a, b).

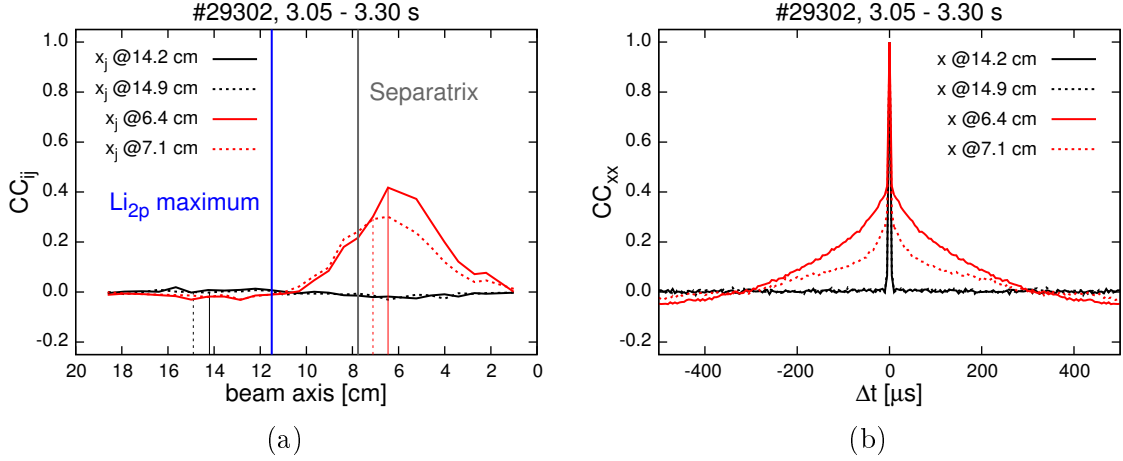


Figure 6.9: Cross and autocorrelation function of the measured line radiation profiles from discharge #29302 3.05-3.30 s (in the same representation as in figure 6.8). The separatrix position is indicated by a grey vertical line. The cross correlation of the measured line radiation shows almost the same shape as the cross correlation of the artificial line radiation (c.f. figure 6.8c).

generated by different lifetimes of the blob-filaments. This observation is mentionable, but not relevant for the following analysis of the blob size, because the blob sizes are only analysed for the time lag $\Delta t = 0$ s. This excludes the temporal distribution from the analysis.

Summarizing, the following points are the main observations, made by comparison of simulated and measured data:

- The applied correlation analysis method can resolve blob filaments, though there is about 50% noise on the signals.
- The assumption of 50% noise on the artificial line radiation time traces lead to similar cross correlation profiles as the measured data.

6.4.5 Relation between width of the emission profile perturbation and the blob size

The simulations from section 6.4.3 (perturbation position μ at 6.40 cm) are now repeated, varying the n_e perturbation width. Thereby, the relation between the n_e perturbation width and the perturbation width in the line radiation profile, which is analysed by the spatial cross correlation function CC_{ij} , is determined. Figure 6.10 shows this dependence for different noise levels and different maximal perturbation amplitudes $\delta n/n$.

The analysis of the line radiation time traces show similar results as the investigations, performed in chapter 4.4. A linear relation between the n_e perturbation width

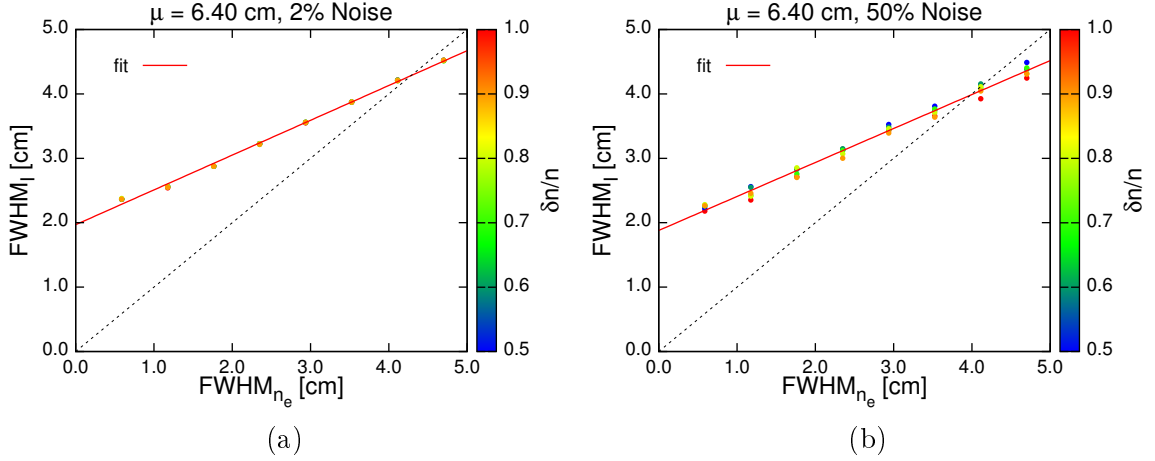


Figure 6.10: Relation between the n_e perturbation width FWHM_{n_e} and the width of the line radiation profile perturbation FWHM_I . The colour scaling indicates the n_e perturbation amplitude $\delta n/n$. For comparison, the black dashed line indicates $\text{FWHM}_{n_e} = \text{FWHM}_I$. The perturbation width of the line radiation profiles, shows linear behaviour (c.f. chapter 4.4), that is almost independent of noise and n_e perturbation amplitude.

FWHM_{n_e} and the emission perturbation width FWHM_I is again observed (c.f. figure 6.10). Additionally, no dependence on the maximal perturbation amplitude $\delta n/n$ is found (c.f. colour scaling). The noise level (comparing figure 6.10a and 6.10b) does not strongly affect the relation.

To calculate original blob sizes from measured line radiation profiles the relation between FWHM_{n_e} and FWHM_I is linearly fitted (red lines, figure 6.10a,b) by the given equation:

$$\text{FWHM}_I = \text{FWHM}_{n_e} \cdot a2 + a1. \quad (6.2)$$

The fit parameter for the different noise levels are found in table 6.3:

noise	a2	a1
2%	$0.540 \pm 0.004 \text{ cm}^{-1}$	$1.96 \pm 0.01 \text{ cm}$
50%	$0.528 \pm 0.007 \text{ cm}^{-1}$	$1.88 \pm 0.02 \text{ cm}$

Table 6.3: Fit parameters

6.4.6 Magnetic field dependence of the blob-filament size

The discharge series, which is described in detail in section 6.4.1, is analysed to determine the dependence of the blob size on the toroidal magnetic field \mathbf{B}_t . From theory, the most stable blob size is given by equation 2.5.

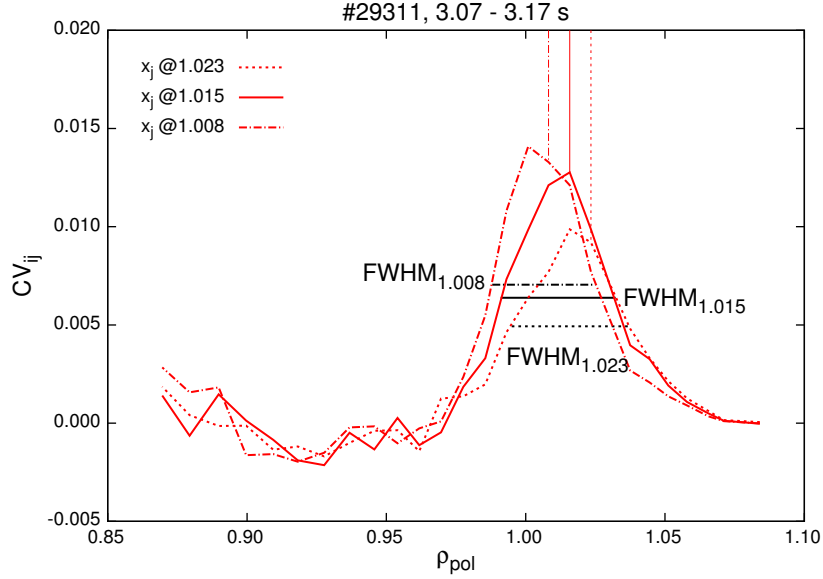


Figure 6.11: Measured blob sizes, using the cross covariance CV_{ij} (c.f. chapter 2.3.1). The reference channels are marked by vertical red lines and the FWHM of each reference channel is indicated by a black horizontal line.

The applied method to analyse the spatial blob size is the cross covariance CV_{ij} (see chapter 2.3.1), because in contrast to the cross correlation function CC_{ij} , it is not normalized to the standard deviation σ of the signals. This is important, because each channel of the new observation system has its own photomultiplier, which possibly has its own noise level. The noise level changes the standard deviation of the signals and therefore, the cross correlation function would be changed.

To determine the blob size three reference channels at $\rho_{pol} = 1.008, 1.015$ and 1.023 are chosen. These channels are indicated at the top of figure 6.11 by red vertical lines. Furthermore, the CV_{ij} profile for all reference channels and their corresponding FWHM is indicated. All reference channels observe almost the same structure size of $FWHM \sim 3.6$ cm.

The investigated discharge series contains the discharges #29302 to #29315. Several time intervals before and after the ‘R_{aus}’ shift (see section 6.4.1) are analysed. The dependence of the blob size on \mathbf{B}_t is shown in figure 6.12. In figure 6.12a the mean, measured line radiation widths $FWHM_l$ are plotted. They are transformed to the blob size $FWHM_{n_e}$ using the inverse of equation 6.2. The corresponding blob sizes are plotted in figure 6.12a. Furthermore, the FWHM of the most stable blob size δ_* , which is described by equation 2.5 (derived in reference [24]), is plotted with a blue dashed line. Table 6.4 shows the parameters, which are used for δ_* . The measured blob sizes do not follow the $B^{-4/5}$ dependence (c.f. equation 2.7). Additionally, the measured blob sizes are about a factor of three larger than the predicted sizes. This

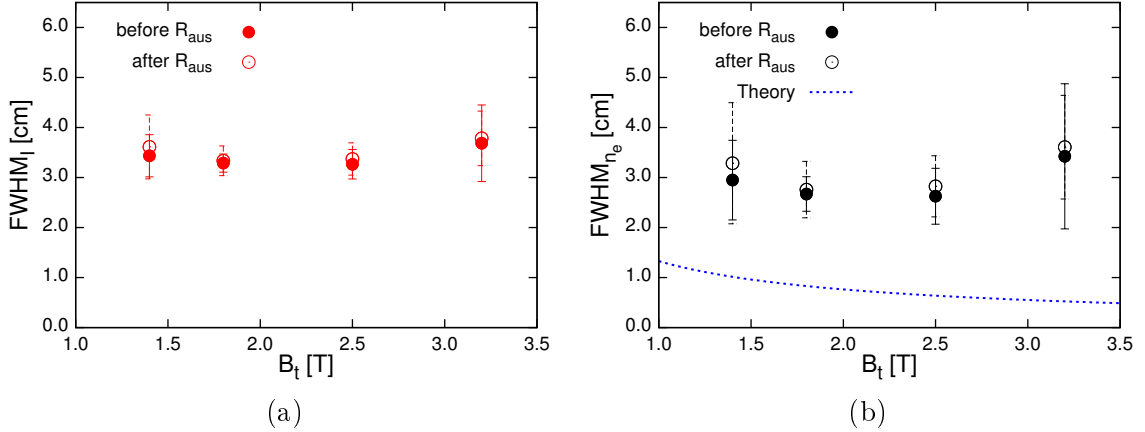


Figure 6.12: Dependence of the blob size on the toroidal magnetic field B_t (reference channels at $\rho_{pol} = 1.008, 1.015$ and 1.023). ‘Before’ or ‘after R_{aus} ’ denotes the analysed time intervals, which are chosen before or after the performed ‘ R_{aus} ’ shift at 2.5 s (c.f. section 6.4.1). Figure (a) includes the width of the analysed line radiation $FWHM_l$. Figure (b) shows calculated blob sizes $FWHM_{r_e}$ from the line radiation widths, using the fitted relation from equation 6.2. The measured blob sizes are larger than the theoretical prediction (blue dashed curve).

parameter	origin	value
magnetic connection length $L_{ }$	mean of the analysed discharges	20.85 m
major plasma radius R	measured	2.13 m
SOL electron temperature T_e	estimated from TS measurement	10 eV

Table 6.4: Parameters for the evaluation of δ_*

huge difference can not easily be explained. The parameters with the largest influence on the most stable blob size δ_* are the electron temperature T_e ($T_e^{2/5}$ dependence) and the connection length $L_{||}$ ($L_{||}^{2/5}$ dependence). $L_{||}$ does not vary strongly, maximally by a factor of 1.5, if different positions along the LB are chosen. The TS measurements of SOL T_e have large errorbars in the range of 100%. The mean estimated 10 eV for T_e are also measured in similarly designed discharges [60]. To increase δ_* to the range of the measured blob sizes, a T_e , which is a factor seven larger, would be required. This seems to be unrealistic and is in contradiction to SOL T_e measurements. A possibility for higher temperatures is that there is also an influence of the ion temperature T_i on δ_* . A method to measure T_i in the SOL is lithium beam activated charge exchange spectroscopy (Li-CXS) [61, 62]. Unfortunately, this measurement is not performed for this discharge series. In retarding field analyser (RFA) measurements, T_i in the SOL is several factors higher than T_e [63, 64]. If the blob size is also dependent on T_i , this could possibly fill parts of the gap between theory and measurement.

Chapter 7

Summary

7.1 Main results

The first part of this section presents the essential results of the simulations, giving a global impression of the capabilities of the LB diagnostic. Second, the physical investigations on plasma turbulence, specifically on the size of blob-filaments, are summarized and discussed.

7.1.1 Capabilities of the LB diagnostic

The following observations are made by the simulation of artificial LB diagnostic data:

- The resolvability of n_e perturbations is dependent on the perturbation position relative to the attenuation of the LB. In front of the line radiation profile maximum, perturbations are well resolvable in space. Here, a positive n_e perturbation leads to an increase of the occupation number of the Li(2p) state, which corresponds to an increase in the line radiation profile. Behind the maximum no spatial resolution is possible because the de-population of the Li(2p) state dominates here. Only perturbations with large amplitudes affect the line radiation profiles, leading to a decrease of the line radiation owing to the stronger de-population of the Li(2p) state and the attenuation of the beam (see chapter 4.2).
- In front of the line radiation profile maximum, where the ground state is well populated, the relation between n_e perturbation amplitude (or size) and perturbation amplitude (or size) in the line radiation profile is almost linear (see chapter 4.3, 4.4).
- The Richardson-Lucy Deconvolution enables a reconstruction of n_e perturbation parameters directly from line radiation profiles. The perturbation position, width and amplitude can be recovered by the application of this method (see

chapter 5).

7.1.2 Blob size analysis

Following analyses of blob sizes are performed:

- The Richardson-Lucy deconvolution is applied to conditionally averaged measured line radiation profiles and its abilities are successfully demonstrated (see chapter 6.2).
- Blob sizes are determined by means of a cross correlation (respectively covariance) analysis and the dependence of the size on \mathbf{B}_t is investigated by the analysis of a discharge series (see chapter 6.4).

The Richardson-Lucy deconvolution and the cross correlation analysis consistently measure blob-filaments with a mean FWHM of about 3 cm, which is significantly larger than estimations from theory. The theoretically predicted sizes are in the range of one centimetre, which is a factor of three smaller than the measurements. Furthermore, the theoretically derived $B^{-4/5}$ dependence of the most stable blob size is not observable.

7.2 Future perspectives

One big goal is to develop a data analysis tool, which enables the direct measurement of blob sizes from Li I ($2p \rightarrow 2s$) line radiation profiles. For this purpose, measured n_e profiles can be used as input for the sensitivity study, which automatically simulates n_e perturbations with amplitude and width in the range of the measured perturbation. From these simulations, the relation between n_e perturbation parameters and line radiation perturbation parameters, can then be extracted, allowing an exact evaluation of the parameters from the actually measured n_e perturbation.

The Richardson-Lucy deconvolution can be further improved. It could be a powerful tool to directly analyse line radiation profiles. Here, two main issues have to be solved. The interpolation of the regular grid has to be optimized and the influences of this interpolation have to be investigated in detail. Furthermore, the influence of noisy line radiation profiles have to be studied. If the method is applied to line radiation profiles, sampled with high frequency, possibilities to reduce noise have to be considered.

Another possibility to remove the Li(2p) lifetime induced smearing from the line radiation profiles, is to utilize a Na beam instead of the Li beam. Here, the lifetime of the excited state is shorter, leading to less smearing. This results in a better spatial accuracy of the line radiation profile.

To explain the deviation of the observed blob sizes from the theoretically predicted ones, the influence of the ion temperature on the most stable blob size has to be

considered [65]. In the SOL the ion temperature can be significantly larger than the electron temperature. The investigation of this hypothesis will be the topic of further experiments.

Acronyms

ASDEX Upgrade axial symmetric divertor experiment upgrade

BES beam emission spectroscopy

BPT bayesian probability theory

B_t toroidal magnetic field

B_θ poloidal magnetic field

D deuterium

DCN deuterium cyanide laser interferometry

ECRH electron cyclotron resonance heating

ELM edge localized mode

ETB edge transport barrier

FWHM full width at half maximum

GPI gas puff imaging

H hydrogen

H-mode high confinement mode

³He helium-3

⁴He helium

IDL Interactive Data Language

IPP Max Planck Institute for Plasma Physics

ITER the Latin word for "the way", a large tokamak constructed in Cadarache, France

L-mode low confinement mode

LB lithium beam

Li lithium

Li-BES lithium beam emission spectroscopy

Li-CXS lithium beam activated charge exchange spectroscopy

Li-IXS lithium beam impact excitation spectroscopy

LFS low field side

LOS lines of sight

MAST mega ampere spherical tokamak

MHD magnetohydrodynamic

n_e electron density

Na sodium

NBI neutral beam injection

NSTX national spherical torus experiment

PFC plasma facing component

P_{heat} heating power

PSF point spread function

RFA retarding field analyser

SIO serial in and output

SOL scrape off layer

T tritium

TEXTOR tokamak experiment for technology oriented research

TS Thomson scattering

Acknowledgement

An dieser Stelle findet sich eine Danksagung, da das Verfassen dieser Arbeit erst durch die Mithilfe und Unterstützung vieler Personen ermöglicht wurde. Es sind so viele, dass es mir leider nicht möglich ist sie alle hier namentlich zu nennen. Darum möchte ich mich beim gesamten *ASDEX Upgrade Team* in Garching und der *AG Aumayr* in Wien für die Zusammenarbeit und das angenehme Arbeitsklima bedanken.

Im Besonderen geht mein Dank an:

Meinen Betreuer, *Friedrich Aumayr*, der mir die Stelle zu dieser Diplomarbeit angeboten hat. Er hat mir Offenheit und Vertrauen entgegengebracht, sowie meine Forschungsaufenthalte am IPP in Garching finanziert. Des Weiteren durfte ich durch seine finanzielle Unterstützung auch Teile der Ergebnisse dieser Arbeit auf der DPG Frühjahrstagung 2013 in Jena präsentieren, was für mich eine bisher einzigartige Erfahrung war.

Meine Betreuerin, *Elisabeth Wolfrum*, die mich sehr liebenswürdig in ihrer Arbeitsgruppe in Garching aufgenommen hat. Neben einer erstklassigen fachlichen Betreuung, die sie mit viel Engagement betrieb, hat sie sich auch besonders menschlich um mich gesorgt. Ihr war wichtig, dass ich mich auch in meiner Freizeit wohl fühle. So wurde mir von ihr z.B. ein Fahrrad zur Verfügung gestellt, damit ich die Gegend in und rund um Garching erkunden konnte.

Meine beiden Co-Betreuer und Mitstreiter, *Gregor Birkenmeier* und *Matthias Wilensdorfer*, für die tagtägliche Unterstützung bei den kleinen und großen Problemen der Experimentalphysik. Außerdem, boten sie mir immer ein offenes Ohr für meine Fragen, investierten viel ihrer Zeit für die Beantwortung dieser und unterstützten mich beim Korrigieren dieser Arbeit.

Meine Bürokollegen in Garching, *Andreas Burckhart*, *Bernhard Sieglin* und *Christian Vorpahl*, die mir bei Schwierigkeiten mit der anfangs ungewohnten IPP-Infrastruktur weitergeholfen haben. Auch durch die Diskussion von anderen spannenden Themen haben sie mir einen angenehmen Arbeitsalltag bereitet.

Meine Bürokollegin in Wien, *Elisabeth Gruber*, mit der ich so wunderbar, auf gut österreichisch gesagt, „Schmäh führen“ kann und die ständig für ansprechende Musik im Büro gesorgt hat.

Meine Freunde, *Anna Galler*, *Bernhard Berger*, *Roland Bliem* und *Thomas Hausma-*

ninger, die mich durch mein Studium begleitet haben und mit denen sich aus einer anfänglichen Lerngruppe eine tiefe private Freundschaft entwickelt hat.

Meine Freunde aus Schul- und Bundesheerzeit, *Bernhard Loitsch* und *Martin Humnig*, da sich unsere Wege wieder in München getroffen haben und somit für genug Freizeitaktivitäten und Geschichten von „damals“ gesorgt war.

Abschließend möchte ich auch noch meiner Familie danken. Sie waren zwar nicht alle an der Entstehung dieser Arbeit direkt beteiligt, doch haben sie mich im ersten Vierteljahrhundert meines Lebens entscheidend geprägt. Ihnen gebührt ein großes Dankeschön:

Meinen Eltern, *Ingrid* und *Martin Laggner*; erst durch ihre finanzielle Unterstützung wurde es mir möglich dieses Studium zu absolvieren, doch es war weit mehr als Geld, das sie mir gegeben haben.

Meinen Geschwistern, *Franziska*, *Peter* und *Thomas Laggner*; mit ihnen bin ich groß geworden, habe mit ihnen Zimmer und Spielsachen geteilt und durfte eine wunderbare Kindheit erleben, die ich nicht missen möchte.

Meiner Freundin, *Caroline Moosmüller*; sie hat mir gezeigt, dass es auch wichtigere Dinge im Leben gibt. Außerdem, unterstützte sie mich bei meinen Plänen, den Weg ins Ausland zu beschreiten und war stets mein Fels in der Brandung. 🐾

DANKE

Bibliography

- [1] Houghton J., ‘Global warming’, *Reports on Progress in Physics*, **68**, 1343 (2005)
- [2] Miley G.H., Towner H. and Ivich N., ‘Fusion cross sections and reactivities’, (1974)
- [3] Bosch H.S. and Hale G., ‘Improved formulas for fusion cross-sections and thermal reactivities’, *Nuclear Fusion*, **32**, 611 (1992)
- [4] Lawson J.D., ‘Some Criteria for a Power Producing Thermonuclear Reactor’, *Proceedings of the Physical Society. Section B*, **70**, 6 (1957)
- [5] Keefe D., ‘Inertial Confinement Fusion’, *Annual Review of Nuclear and Particle Science*, **32**, 391 (1982)
- [6] ‘European Fusion Development Agreement’, (2013), URL <http://www.efda.org/2011/09/tokamak-principle-2/>
- [7] ‘European Fusion Development Agreement’, (2013), URL <http://www.efda.org/wpcms/wpcontent/uploads/2011/07/fig05.jpg?f81117>
- [8] ‘Detailed description of ASDEX Upgrade’, (2013), URL <https://www.aug.ipp.mpg.de/wwwaug/documentation/physics/techdata.shtml>
- [9] Wagner F., Becker G., Behringer K., Campbell D., Eberhagen A., Engelhardt W., Fussmann G., Gehre O., Gernhardt J., Gierke G., Haas G., Huang M., Karger F., Keilhacker M., Klüber O., Kornherr M., Lackner K., Lisitano G., Lister G., Mayer H., Meisel D., Müller E., Murmann H., Niedermeyer H., Poschenrieder W., Rapp H. and Röhr H., ‘Regime of Improved Confinement and High Beta in Neutral-Beam-Heated Divertor Discharges of the ASDEX Tokamak’, *Physical Review Letters*, **49**, 1408 (1982)
- [10] Wagner F., Fussmann G., Grave T., Keilhacker M., Kornherr M., Lackner K., McCormick K., Müller E., Stäbler A., Becker G., Bernhardt K., Ditte U., Eberhagen A., Gehre O., Gernhardt J., Gierke G., Glock E., Gruber O., Haas G., Hesse M., Janeschitz G., Karger F., Kissel S., Klüber O., Lisitano G., Mayer H. and Meisel D., ‘Development of an Edge Transport Barrier at the H-Mode Transition of ASDEX’, *Physical Review Letters*, **53**, 1453 (1984)

- [11] Schneider P.A., Wolfrum E., Groebner R., Osborne T.H., Beurskens M., Dunne M.G., Ferron J.R., Günter S., Kurzan B., Lackner K., Snyder P.B., Zohm H., the ASDEX Upgrade Team, the DIII-D Team and JET-EFDA Contributors, ‘Differences in the H-mode pedestal width of temperature and density’, *Plasma Physics and Controlled Fusion*, **54**, 105009 (2012)
- [12] Willensdorfer M., Wolfrum E., Fischer R., Schweinzer J., Sertoli M., Sieglin B., Veres G., Aumayr F. and the ASDEX Upgrade Team, ‘Improved chopping of a lithium beam for plasma edge diagnostic at ASDEX Upgrade’, *Review of Scientific Instruments*, **83**, 023501 (2012)
- [13] Willensdorfer M., ‘Temporal behavior of the plasma edge density throughout the L-H transition in ASDEX Upgrade’, Ph.D. thesis, Technische Universität Wien (2013)
- [14] D’Ippolito D.A., Myra J.R. and Zweben S.J., ‘Convective transport by intermittent blob-filaments: Comparison of theory and experiment’, *Physics of Plasmas*, **18** (2011)
- [15] Groebner R., Leonard A., Osborne T., Porter G., Colchin R. and Owen L., ‘The role of neutrals in high-mode (H-mode) pedestal formation’, *Physics of Plasma*, **9**, 2134 (2002)
- [16] Stroth U., ‘Transport in Toroidal Plasmas’, in A. Dinklage, T. Klinger, G. Marx and L. Schweikhard, eds., *Plasma Physics*, volume 670 of *Lecture Notes in Physics*, 213–267, Springer Berlin Heidelberg (2005)
- [17] Stroth U., *Plasmaphysik*, Vieweg+Teubner (2011)
- [18] Kirk A., Ayed N.B., Counsell G., Dudson B., Eich T., Herrmann A., Koch B., Martin R., Meakins A., Saarelma S., Scannell R., Tallents S., Walsh M., Wilson H.R. and the MAST Team, ‘Filament structures at the plasma edge on MAST’, *Plasma Physics and Controlled Fusion*, **48**, B433 (2006)
- [19] Krasheninnikov S., ‘On scrape off layer plasma transport’, *Physics Letters A*, **283**, 368 (2001)
- [20] D’Ippolito D.A., Myra J.R. and Krasheninnikov S.I., ‘Cross-field blob transport in tokamak scrape-off-layer plasmas’, *Physics of Plasmas*, **9**, 222 (2002)
- [21] D’Ippolito D.A., Myra J.R., Krasheninnikov S.I., Yu G.Q. and Pigarov A.Y., ‘Blob Transport in the Tokamak Scrape-off-Layer’, *Contributions to Plasma Physics*, **44**, 205 (2004)
- [22] Rhodes T., Ritz C. and Bengtson R., ‘Scaling of far edge plasma turbulence and fluctuation induced particle transport in the TEXT tokamak’, *Nuclear Fusion*, **33**, 1147 (1993)
- [23] McKee G., Petty C., Waltz R., Fenzi C., Fonck R., Kinsey J., Luce T., Burrell K., Baker D., Doyle E., Garbet X., Moyer R., Rettig C., Rhodes T., Ross D., Staebler G., Sydora R. and Wade M., ‘Non-dimensional scaling of turbulence

- characteristics and turbulent diffusivity', *Nuclear Fusion*, **41**, 1235 (2001)
- [24] Krasheninnikov S.I., D'Ippolito D.A. and Myra J.R., 'Recent theoretical progress in understanding coherent structures in edge and SOL turbulence', *Journal of Plasma Physics*, **74** (2008)
- [25] Sugita S., Yagi M., Itoh S.I. and Itoh K., 'Propagation Velocity Analysis of a Single Blob in the SOL', *Plasma and Fusion Research*, **3**, 040 (2008)
- [26] Zohm H., 'Edge localized modes (ELMs)', *Plasma Physics and Controlled Fusion*, **38**, 105 (1996)
- [27] Migliucci P., Naulin V. and JET-EFDA Contributors, 'Magnetic signature of current carrying edge localized modes filaments on the Joint European Torus tokamak', *Physics of Plasmas*, **17**, 072507 (2010)
- [28] Zweben S.J., Boedo J.A., Grulke O., Hidalgo C., LaBombard B., Maqueda R.J., Scarin P. and Terry J.L., 'Edge turbulence measurements in toroidal fusion devices', *Plasma Physics and Controlled Fusion*, **49**, S1 (2007)
- [29] LaBombard B., 'An interpretation of fluctuation induced transport derived from electrostatic probe measurements', *Physics of Plasmas*, **9**, 1300 (2002)
- [30] Boedo J.A., Rudakov D., Moyer R., Krasheninnikov S., Whyte D., McKee G., Tynan G., Schaffer M., Stangeby P., West P., Allen S., Evans T., Fonck R., Hollmann E., Leonard A., Mahdavi A., Porter G., Tillack M. and Antar G., 'Transport by intermittent convection in the boundary of the DIII-D tokamak', *Physics of Plasmas*, **8**, 4826 (2001)
- [31] Huber A., Samm U., Schweer B. and Mertens P., 'Results from a double Li-beam technique for measurement of both radial and poloidal components of electron density fluctuations using two thermal beams', *Plasma Physics and Controlled Fusion*, **47**, 409 (2005)
- [32] Terry J.L., Zweben S.J., Hallatschek K., LaBombard B., Maqueda R.J., Bai B., Boswell C.J., Greenwald M., Kopon D., Nevins W.M., Pitcher C.S., Rogers B.N., Stotler D.P. and Xu X.Q., 'Observations of the turbulence in the scrape-off-layer of Alcator C-Mod and comparisons with simulation', *Physics of Plasmas*, **10**, 1739 (2003)
- [33] Maqueda R., Stotler D. and the NSTX Team, 'Intermittent divertor filaments in the National Spherical Torus Experiment and their relation to midplane blobs', *Nuclear Fusion*, **50**, 075002 (2010)
- [34] Birkenmeier G., 'Experimentelle Untersuchungen zur Struktur und Dynamik von Driftwellenturbulenz in Stellaratorgeometrie', Ph.D. thesis, Universität Stuttgart (2012)
- [35] Ramisch M., 'Scaling and Manipulation of Turbulent Structures in the Torsatron TJ-K', Ph.D. thesis, Christian-Albrechts-Universität zu Kiel (2005)

- [36] Huld T., Nielsen A.H., Pécseli H.L. and Rasmussen J.J., 'Coherent structures in two-dimensional plasma turbulence', *Physics of Fluids B: Plasma Physics*, **3**, 1609 (1991)
- [37] Zoletnik S., Fiedler S., Kocsis G., McCormick G.K., Schweinzer J. and Winter H.P., 'Determination of electron density fluctuation correlation functions via beam emission spectroscopy', *Plasma Physics and Controlled Fusion*, **40**, 1399 (1998)
- [38] Johnsen H., Pécseli H.L. and Trulsen J., 'Conditional eddies in plasma turbulence', *Physics of Fluids*, **30**, 2239 (1987)
- [39] Aumayr F. and Winter H., 'Plasmadiagnostik mit Lithiumatomstrahl-aktivierter Umladungsspektroskopie', *Annalen der Physik*, **497**, 228 (1985)
- [40] Thomas D.M., Hyatt A.W. and Thomas M.P., 'Edge density fluctuation diagnostic for DIII-D using lithium beams', *Review of Scientific Instruments*, **61**, 3040 (1990)
- [41] Schorn R., Hintz E., Rusbüldt D., Aumayr F., Schneider M., Unterreiter E. and Winter H., 'Absolute concentrations of light impurity ions in tokamak discharges measured with lithium-beam-activated charge-exchange spectroscopy', *Applied Physics B*, **52**, 71 (1991)
- [42] Schweinzer J., Wolfrum E., Aumayr F. and Pöckl M., 'Reconstruction of Plasma Edge Density Profiles from LiI (2s-2p) Emission Profiles', *Plasma Physics and Controlled Fusion*, **34**, 1173 (1992)
- [43] Wolfrum E., Aumayr F., Wutte D., Winter H. and Hintz E., 'Fast lithium-beam spectroscopy of tokamak edge plasmas', *Review of Scientific Instruments*, **64**, 8 (1993)
- [44] Fiedler S., Brandenburg R., Baldzuhn J., McCormick K., Aumayr F., Schweinzer J. and Winter H., 'Edge plasma diagnostics on W7-AS and ASDEX-Upgrade using fast Li beams', *Journal of Nuclear Materials*, **266?269**, 1279 (1999)
- [45] Brandenburg R., Schweinzer J., Fiedler S. and Aumayr F., 'Modelling of fast neutral Li beams for fusion edge plasma diagnostics', *Plasma Physics and Controlled Fusion*, **41**, 471 (1999)
- [46] Brandenburg R., Aumayr F., Winter H., Petravich G., Zoletnik S., Fiedler S., McCormick K., Schweinzer J. and the W7-AS and ASDEX Upgrade Teams, 'Fast lithium beam edge plasma spectroscopy at IPP Garching - Status and recent developments', *Fusion Science and Technology*, **36**, 289 (1999)
- [47] Fischer R., Wolfrum E. and Schweinzer J., 'Probabilistic lithium beam data analysis', *Plasma Physics and Controlled Fusion*, **50**, 085009 (2008)
- [48] Brix M., Dodt D., Dunai D., Lupelli I., Marsen S., Melson T.F., Meszaros B.,

- Morgan P., Petravich G., Refy D.I., Silva C., Stamp M., Szabolics T., Zastrow K.D., Zoletnik S. and JET-EFDA Contributors, 'Recent improvements of the JET lithium beam diagnostic', *Review of Scientific Instruments*, **83**, (2012)
- [49] Behler K., Blank H., Buhler A., Cole R., Drube R., Engelhardt K., Eixenberger H., Hicks N., Lohs A., Lüddecke K., Mlynek A., Mszanowski U., Merkel R., Neu G., Raupp G., Reich M., Suttrop W., Treutterer W. and Zilker M., 'Real-time standard diagnostic for {ASDEX} Upgrade', *Fusion Engineering and Design*, **85**, 313 (2010)
- [50] Willensdorfer M., Birkenmeier G., Fischer R., Laggner F.M., Wolfrum E., Veres G., Aumayr F., Carralero D., Kobayashi T. and the ASDEX Upgrade Team, 'Characterization of the lithium beam emission spectroscopy at ASDEX Upgrade', *accepted in Plasma Physics and Controlled Fusion* (2013)
- [51] Schweinzer J., Brandenburg R., Bray I., Hoekstra R., Aumayr F., Janev R. and Winter H., 'DATABASE FOR INELASTIC COLLISIONS OF LITHIUM ATOMS WITH ELECTRONS, PROTONS, AND MULTIPLY CHARGED IONS', *Atomic Data and Nuclear Data Tables*, **72**, 239 (1999)
- [52] Wiese W.L., Smith M.W. and Miles B.M., *Atomic Transition Probabilities*, NSRDS- NBS 22. U.S.A. National Bureau of Standards, Washington DC (1969)
- [53] Kallenbach A., Dux R., Gafert J., Haas G., Horton L., Jakobi M., Kurzan B., Müller H., Neu R., Neuhauser J., Pugno R., Pütterich T., Rohde V., Sandmann W., Yoon S.W. and the ASDEX Upgrade Team, 'Edge transport and its interconnection with main chamber recycling in ASDEX Upgrade', *Nuclear Fusion*, **43**, 573 (2003)
- [54] Wolfrum E., Schweinzer J., Bridi D., Igenbergs K., Kamleitner J. and Aumayr F., 'A sodium (Na) beam edge diagnostic', *Journal of Nuclear Materials*, **390-391**, 1110 (2009)
- [55] Igenbergs K., Schweinzer J., Bray I., Bridi D. and Aumayr F., 'Database for inelastic collisions of sodium atoms with electrons, protons, and multiply charged ions', *Atomic Data and Nuclear Data Tables*, **94**, 981 (2008)
- [56] Richardson W.H., 'Bayesian-Based Iterative Method of Image Restoration', *J. Opt. Soc. Am.*, **62**, 55 (1972)
- [57] Lucy L.B., 'An iterative technique for the rectification of observed distributions', *The Astronomical Journal*, **79**, 745 (1974)
- [58] 'Interactive Data Language', (2013), URL <http://www.exelisvis.com/ProductsServices/IDL.aspx>
- [59] Mlynek A., Reich M., Giannone L., Treutterer W., Behler K., Blank H., Buhler A., Cole R., Eixenberger H., Fischer R., Lohs A., Lüddecke K., Merkel R., Neu G., Ryter F., Zasche D. and the ASDEX Upgrade Team, 'Real-time feedback control of the plasma density profile on ASDEX Upgrade', *Nuclear Fusion*, **51**,

- 043002 (2011)
- [60] Nold B., Conway G.D., Happel T., Müller H.W., Ramisch M., Rohde V., Stroth U. and the ASDEX Upgrade Team, ‘Generation of blobs and holes in the edge of the ASDEX Upgrade tokamak’, *Plasma Physics and Controlled Fusion*, **52**, 065005 (2010)
- [61] Schorn R., Wolfrum E., Aumayr F., Hintz E., Rusbult D. and Winter H., ‘Radial temperature distributions of C 6+ ions in the TEXTOR edge plasma measured with lithium beam activated charge exchange spectroscopy’, *Nuclear Fusion*, **32**, 351 (1992)
- [62] Reich M., Wolfrum E., Schweinzer J. and Ehmler H., ‘Edge ion temperature diagnostic for ASDEX Upgrade’, *Plasma Physics and Controlled Fusion*, **46**, 797 (2004)
- [63] Kočan M., Pánek R., Stöckel J., Hron M., Gunn J. and Dejarnac R., ‘Ion temperature measurements in the tokamak scrape-off layer’, *Journal of Nuclear Materials*, **363-365**, 1436 (2007)
- [64] Kočan M., Gunn J.P., Pascal J.Y., Bonhomme G., Fenzi C., Gauthier E. and Segui J.L., ‘Edge ion-to-electron temperature ratio in the Tore Supra tokamak’, *Plasma Physics and Controlled Fusion*, **50**, 125009 (2008)
- [65] Manz P., Carralero D., Birkenmeier G., Müller H.W., Müller S.H., Fuchert G., Scott B.D. and Stroth U., ‘Filament velocity scaling laws for warm ions’, *Physics of Plasmas*, **20**, (2013)